Received: 10 July 2018 | Revised: 24 September 2018 | Accepted: 1 October 2018
DOI: 10.1002/glia.23549

GLIA
WILEY

RESEARCH ARTICLE

Maintenance of high proteolipid protein level in adult central nervous system myelin is required to preserve the integrity of myelin and axons

Katja A. Lüders[1,2] | Stefan Nessler[3] | Kathrin Kusch[1] | Julia Patzig[1] | Ramona B. Jung[1] | Wiebke Möbius[1,4] | Klaus-Armin Nave[1,4] | Hauke B. Werner[1]

[1]Department of Neurogenetics, Max Planck Institute of Experimental Medicine, Göttingen, Germany

[2]Göttingen Graduate School for Neurosciences, Biophysics and Molecular Biosciences, Göttingen, Germany

[3]Institute of Neuropathology, University Medical Center Göttingen, Göttingen, Germany

[4]Center for Nanoscale Microscopy and Molecular Physiology of the Brain, Göttingen, Germany

Correspondence
Hauke Werner, Max Planck Institute of Experimental Medicine, Hermann-Rein-Str. 3; D-37075 Göttingen, Germany.
Email: hauke@em.mpg.de
and
Klaus-Armin Nave, Max Planck Institute of Experimental Medicine, Hermann-Rein-Str. 3; D-37075 Göttingen, Germany.
Email: nave@em.mpg.de

Funding information
Deutsche Forschungsgemeinschaft (DFG), Grant/Award Numbers: WE 2720/4-1 and WE 2720/2-2 to HBW; European Research Council (ERC): Advanced Grant to KAN; Cluster of Excellence and Deutsche Forschungsgemeinschaft (DFG) Research Center Nanoscale Microscopy and Molecular Physiology of the Brain

Abstract

Proteolipid protein (PLP) is the most abundant integral membrane protein in central nervous system (CNS) myelin. Expression of the *Plp*-gene in oligodendrocytes is not essential for the biosynthesis of myelin membranes but required to prevent axonal pathology. This raises the question whether the exceptionally high level of PLP in myelin is required later in life, or whether high-level PLP expression becomes dispensable once myelin has been assembled. Both models require a better understanding of the turnover of PLP in myelin in vivo. Thus, we generated and characterized a novel line of tamoxifen-inducible *Plp*-mutant mice that allowed us to determine the rate of PLP turnover after developmental myelination has been completed, and to assess the possible impact of gradually decreasing amounts of PLP for myelin and axonal integrity. We found that 6 months after targeting the *Plp*-gene the abundance of PLP in CNS myelin was about halved, probably reflecting that myelin is slowly turned over in the adult brain. Importantly, this reduction by 50% was sufficient to cause the entire spectrum of neuropathological changes previously associated with the developmental lack of PLP, including myelin outfoldings, lamellae splittings, and axonal spheroids. In comparison to axonopathy and gliosis, the infiltration of cytotoxic T-cells was temporally delayed, suggesting a corresponding chronology also in the genetic disorders of PLP-deficiency. High-level abundance of PLP in myelin throughout adult life emerges as a requirement for the preservation of white matter integrity.

KEYWORDS

glia-axonal support, myelin turnover, neuropathology, oligodendrocyte, proteolipid protein (PLP), spastic paraplegia, tamoxifen

1 | INTRODUCTION

In the CNS of vertebrates, saltatory transmission of nerve impulses (Tasaki, 1939) along axons is facilitated by their spiral enwrapment by oligodendroglial processes, which form electrically insulating myelin sheaths (Kruger & Maxwell, 1966; Nave & Werner, 2014). The major protein of CNS myelin is a lipid-associated transmembrane-tetraspan termed proteolipid protein (PLP) (Folch & Lees, 1951; Krämer-Albers, Gehrig-Burger, Thiele, Trotter, & Nave, 2006; Milner et al., 1985; Möbius, Patzig, Nave, & Werner, 2008; Simons, Kramer, Thiele, Stoffel, & Trotter, 2000; Werner et al., 2013). Expression of the *Plp*-gene (official gene name *Plp1*) is highly enriched in oligodendrocytes (Lüders, Patzig, Simons, Nave, & Werner, 2017; Trapp et al., 1987). Complete deficiency of PLP in $Plp^{null/Y}$ mice impairs the rate of myelination (de Monasterio-Schrader et al., 2013; Yool et al., 2001), the ultrastructure of myelin (Klugmann et al., 1997; Patzig, Erwig, et al., 2016), the abundance in myelin of cholesterol, the deacetylase sirtuin-2 and filament-forming septins (Patzig, Erwig, et al., 2016; Werner et al., 2007; Werner et al., 2013), axonal integrity (Edgar et al., 2004; Griffiths et al., 1998) as well as motor capabilities (Gould et al., 2018;

Griffiths et al., 1998; Janova et al., 2018; Petit et al., 2014). By quantitative mass spectrometry, PLP constitutes >15% of the total protein in myelin biochemically purified from healthy mouse brains (de Monasterio-Schrader et al., 2012; Jahn, Tenzer, & Werner, 2009; Werner et al., 2013), an exceptionally high level of abundance. Indeed, when assessing entire mouse brain, PLP is among the most abundant transmembrane proteins (Sharma et al., 2015). However, the functional relevance of the exceptionally high PLP content of CNS myelin remained unknown.

Functional myelin can also be formed with low amounts of PLP. Indeed, PLP is only a minor constituent of PNS myelin (Patzig et al., 2011; Yoshida & Colman, 1996) and of CNS myelin in fish (Franz, Waehneldt, Neuhoff, & Wachtler, 1981; Kirschner, Inouye, Ganser, & Mann, 1989; Waehneldt, 1990; Yoshida & Colman, 1996). Notably, PLP replaced the adhesion molecule myelin protein zero (P0/MPZ) as the major constituent of CNS myelin at the evolutionary transition from fish to tetrapods (Yoshida & Colman, 1996). Interestingly, transgenic mice that express P0 instead of PLP in CNS myelin display axonal degeneration (Yin et al., 2006) similar to $Plp^{null/Y}$ mice (Griffiths et al., 1998), suggesting that the P0-to-PLP shift in ancestral tetrapods provided oligodendrocytes with the capacity to support the energy metabolism and thus long-term integrity of axons (Philips & Rothstein, 2017; Saab, Tzvetanova, & Nave, 2013).

Similar to $Plp^{null/Y}$ mice, patients with spastic paraplegia (SPG2) caused by a *null*-allele of the *PLP1*-gene display prominent axonal degeneration (Garbern et al., 2002) but only moderate hypomyelination (Garbern et al., 1997). Importantly, PLP-related axonal pathology is a local phenomenon of individual axon/myelin-units. This became evident when the precise distribution of axonal spheroids was analyzed in female heterozygous mice (genotype $Plp^{+/-}$) (Edgar et al., 2004), in which PLP-deficient oligodendrocytes and myelin sheaths neighbor those with normal PLP-expression due to random inactivation of the X-chromosomal *Plp*-gene (Yool et al., 2001). Indeed, the spheroids were essentially associated with PLP-deficient myelin sheaths but did not spread to adjacent PLP-containing internodes (Edgar et al., 2004). These experiments have corroborated the existence of a PLP-dependent function of myelinating oligodendrocytes in locally preserving the integrity of their myelinated axons; however, they have not addressed the functional relevance of the very high PLP-content of CNS myelin.

Here, we scrutinize the pathobiological consequences of deleting the *Plp*-gene in mature oligodendrocytes in adult mice. The abundance of PLP in CNS myelin is halved about six months after terminating its replenishment, probably reflecting its slow turnover. Importantly, this reduction is sufficient to cause all known neuropathological facets of PLP-related disorders, including hypomyelination, altered myelin ultrastructure and axonal pathology. The chronology of the emerging neuropathology implies that the onset of the axonopathy precedes the infiltration of cytotoxic T-cells. We propose that the exceptionally high level of PLP-abundance in CNS myelin of tetrapods is subject to selective pressure, which preserves the integrity of myelin and axons and thus a healthy nervous system.

2 | MATERIALS AND METHODS

2.1 | Mouse models

To delete the *Plp* gene in oligodendrocytes in the adult CNS, we used Plp^{flox} mice in which exon 3 of the *Plp* gene is flanked by loxP-sites (Lüders et al., 2017; Wang et al., 2017). Plp^{flox} mice were interbred with mice expressing tamoxifen inducible Cre recombinase under control of the *Plp* promoter ($Plp^{CreERT2}$ mice) (Leone et al., 2003). Mice were injected with tamoxifen intraperitoneally (i.p.) at the age of 8 weeks (1 mg/100 μl corn oil per mouse per day) for 10 days with a break of 2 days after the first five consecutive days of injection. Tamoxifen (Sigma-Aldrich, St. Louis, MO) was dissolved in corn oil (Sigma-Aldrich) and mixed on a vortexer (Heidolph, Schwabach, Germany) in the dark for at least half an hour at RT before injection. Both $Plp^{flox/Y}$ and $Plp^{flox/Y}{*}Plp^{CreERT2}$ mice were injected with tamoxifen and are also referred to as control (Ctrl) and induced conditional knockout (iKO) mice, respectively. Routine genotyping of the Plp^{flox} allele as shown in Figure 1b was performed by genomic PCR using primers 24460 (5′-GACATAGCCC TCAGTGTTCAGG), 24461 (5′-GAATCCTGCA TGGACAGACAG), and 32796 (5′-CACACACATA TTCAGACCCCC). Genotyping of $Plp^{CreERT2}$ mice was with primers 10099 (5′-TGGACAGCTG GGACAAAGTAAGC) and *7963* (5′-CGTTGCATCG ACCGGTAATGCAGGC). Genotyping of $Plp^{null/Y}$ mice (Klugmann et al., 1997) was with primers 1864 (5′-TTGGCGGCGA ATGGGCTGAC), 2729 (5′-GGAGAGGAGG AGGGAAACGAG), and 2731 (5′-TCTGTTTTGC GGCTGACTTTG). Mice were bred and kept in the animal facility of the Max Planck Institute of Experimental Medicine with a 12 hr light/dark cycle and 2–5 mice per cage. All experiments were performed in accordance with the German animal protection law.

2.2 | Quantitative reverse transcriptase-PCR

qRT-PCR was essentially performed as described (de Monasterio-Schrader et al., 2013). Briefly, mice were sacrificed by cervical dislocation, brains were dissected and optic nerves removed. Half brains were homogenized in 0.32 M sucrose containing protease inhibitor (Complete Mini, Roche, Basel, Switzerland) using an Ultraturrax homogenizer (IKA T10 Basic). 20 μl of the homogenate were transferred to RLT buffer (RNeasy Miniprep kit; Qiagen, Hilden, Germany) supplemented with β-mercaptoethanol. RNA extraction and purification was performed using the RNeasy Miniprep kit (Qiagen). Random nonamer primers and Superscript II RNA H Reverse Transcriptase (Invitrogen, Carlsbad, CA) were used to synthesize cDNA. The pipetting robot epMotion 5075 (Eppendorf, Hamburg, Germany) was used for pipetting. qRT-PCR was performed using the Power SYBR Green PCR Master Mix (Applied Biosystems, Foster City, CA) and the Light Cycler 480II (Roche). mRNA abundance was analyzed in relation to the mean of the standards *Ube3l2*, *Rplp0*, and *Rps13*, which did not differ between genotypes. Primers were specific for *Plp* (5′-CTCCAAAAAC TACCAGGACTATGAG and 5′-AGGGCCCCAT AAAGGAAGA), *Mbp* (5′-GCCTCC GTAG CCAAATCC and 5′-AGGGCCCCAT AAAGGAAGA), *Cnp* (5′-CGC TGGGGCA GAAGAATAC and 5′-AAGGCCTTGC CATACGATCT), *Tnfa* (5′-TGCCTATGTC TCAGCCTCTTC and 5′-GAGGCCATTT GGGAAC TTCT), *Ccl2* (5′-GCCTGCTGTT CACAGTTGC and 5′-CAGGTGAGTG

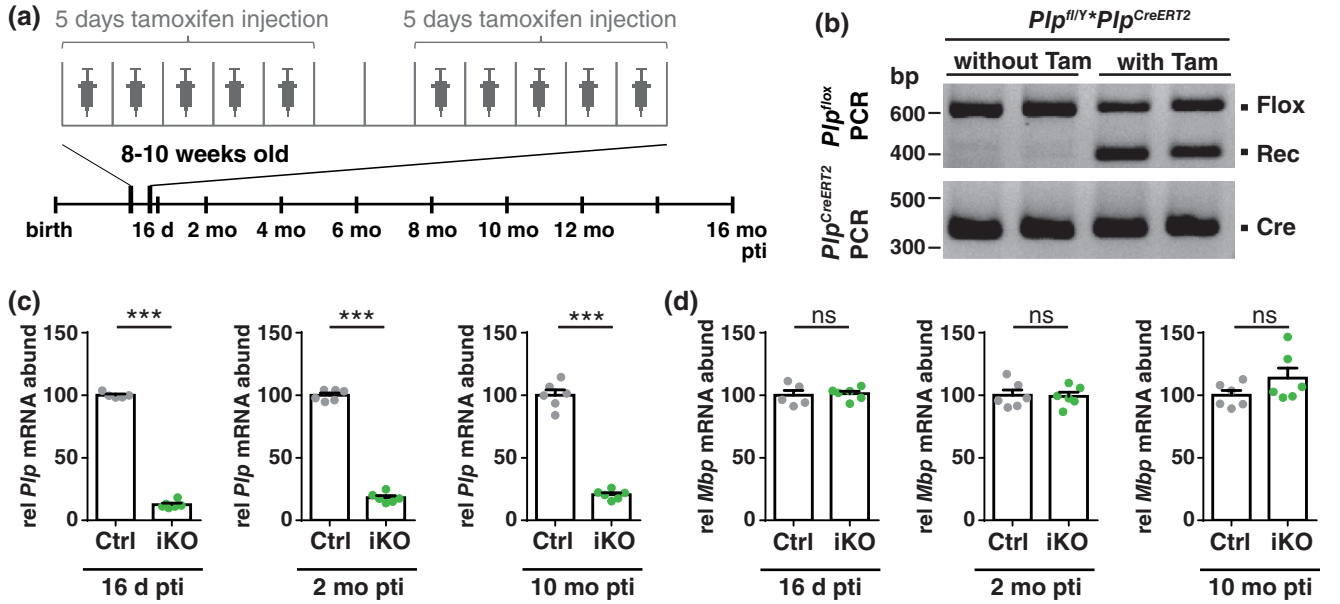

FIGURE 1 Tamoxifen-inducible mouse model of *Plp* deficiency in adult mice. (a) Tamoxifen injection scheme for inactivation of the *Plp* gene. $Plp^{flox/Y}$ (Ctrl) and $Plp^{flox/Y}{*}Plp^{CreERT2}$ (iKO) male mice were injected i.p. with tamoxifen and analyzed at the indicated time points (16 days, 2, 4, 6, 8, 10, 12, and 16 months pti). (b) Genotyping PCR of genomic DNA detects the recombined Plp^{flox} allele (Rec; 462 bp product) after tamoxifen injection, whereas only the non-recombined Plp^{flox} allele (Flox; 683 bp) is observed without tamoxifen injection. (c, d) qRT-PCR to determine the abundance of *Plp* and *Mbp* transcripts in mouse brains. (c) Note that *Plp* mRNA is diminished in iKO mice compared with Ctrl mice at all investigated times points (16 days, 2 and 10 months pti). (d) Conversely there is no significant change in *Mbp* mRNA abundance. pti = post tamoxifen injection; Tam = tamoxifen; mean with *SEM*; $n = 5–6$; two-tailed unpaired *t*-test; $p < .001$ (***)

GGGCGTTA), *Tgfb1* (5′-TGGAGCAACA TGTGGAACTC and 5′-CAGC AGCCGG TTACCAAG), *Il1b* (5′-AGTTGACGGAC CCCAAAAG and 5′-TTTGAAGCTG GATGCTCTCAT), *Il10* (5′-GGTTGCCAAG CCTTATC GGA and 5′-ACCTGCTCCA CTGCCTTGCT), *Il12b* (5′-ATCGTTTTGC TGGTGTCTCC and 5′- GGAGTCCAGT CCACCTCTACA), *Ube3l2* (5′-CACATTTGCG GATCTCTTCA and 5′-AGCAGCACCA GATCCAA-GAT), *Rplp0* (5′-GATGCCCAGG GAAGACAG and 5′-ACAATGAAGC ATTTTGGATAATCA), and *Rps13* (5′-CGAAAGCACC TTGAGAGGAA and 5′-TTCCAATTAG GTGGGAGCAC). Statistical analysis was performed using two-tailed unpaired *t*-test in GraphPad Prism 6.0. Level of significance was set as $p < .001$ (***).

For comparing the abundance of *Plp* mRNA between Ctrl and iKO mice in Figure 1c, *p*-values are $p < .0001$ (16 days pti), $p = .0001$ (2 months pti), and $p = .0001$ (10 months pti). For comparing the abundance of *Mbp* mRNA between Ctrl and iKO mice in Figure 1d, the exact *p*-values are $p = .7729$ (16 days pti), $p = .8771$ (2 months pti), and $p = .1565$ (10 months pti). For comparing the abundance of *Cnp* mRNA between Ctrl and iKO mice in Supporting Information Figure S1c, the exact *p*-value is $p = .6393$. For comparing the abundance of microglial marker mRNAs between Ctrl and iKO mice in Supporting Information Figure S4, the *p*-values are: $p = .0353$ (*Il1b*), $p = .1952$ (*Tnfa*), $p = .1372$ (*Il12b*), $p = .6332$ (*Ccl2*), $p = .7747$ (*Il10*) and $p = .9444$ (*Tgfb1*).

2.3 | Myelin purification and immunoblotting

Purification of a light-weight membrane fraction enriched for myelin was performed as described (Jahn, Tenzer, Bartsch, Patzig, & Werner, 2013; Patzig, Erwig, et al., 2016). Briefly, half brains of three male Ctrl and iKO mice each at 16 days and 2, 4, 6, 8, 10, 12, and 16 months pti were homogenized in 0.32 M sucrose and processed in parallel as described. Purified myelin was taken up in 1x TBS with protease inhibitor (Complete Mini, Roche). Protein concentration was measured using the DC protein assay (BioRad Laboratories, Hercules, CA).

Immunoblotting was essentially performed as described (Kusch et al., 2017; Schardt et al., 2009). Purified myelin (0.8 μg for PLP/DM20; 2.5 μg for MBP; 3 μg for CNP; 10 μg for ATP1a3 and SIRT2) was separated on SDS-polyacrylamide gels (15% for PLP/DM20 and MBP; 10% for ATP1a3 and SIRT2) and blotted onto PVDF membranes (Hybond; Amersham) using the Novex Semi-Dry Blotter (Invitrogen, Carlsbad, CA, USA). Primary antibodies were incubated over night at 4 °C in 50% Odyssey Blocking buffer (LI-COR, Lincoln, NE) in TBS with 0.1% Tween 20. Primary antibodies were specific for PLP/DM20 (A431; 1:5,000; [Jung, Sommer, Schachner, & Nave, 1996]), MBP 18.5 kDa isoform (1:500; Novocastra 7H11), CNP (1:500; Sigma C5922), ATP1A3 (1:1,000; abcam ab2826), and SIRT2 (1:2,500; abcam 67299). Fluorescently coupled secondary antibodies α-rabbit-IRDye800CW (1:2,500; LI-COR P/N 925-32211) and α-mouse-IRDye680RD (1:2,500; LI-COR P/N 925-68070) were incubated in 50% Odyssey Blocking Buffer (LI-COR) in TBS with 0.1% Tween and 0.01% SDS for 1 hr at RT and detected using the Odyssey infrared Imager (LI-COR). Relative intensity of fluorescent bands was measured in relation to the background using Image Studio Ver 3.1 (Li-COR). Graphs were plotted using GraphPad Prism 6.0 and an exponential curve with one phase decay was fitted in Figure 2b,c. Statistical analysis was performed using a two-tailed unpaired *t*-test in GraphPad Prism 6.0 for each individual time point (iKO compared with age-matched Ctrl) in Figure 2b,c and for graphs e, f, and h. Levels of significance were set as $p < .05$ (*), $p < .01$ (**), and $p < .001$ (***).

For comparison of the abundance of PLP in myelin between Ctrl and iKO in Figure 2b *p*-values are $p = .2131$ (16d pti),

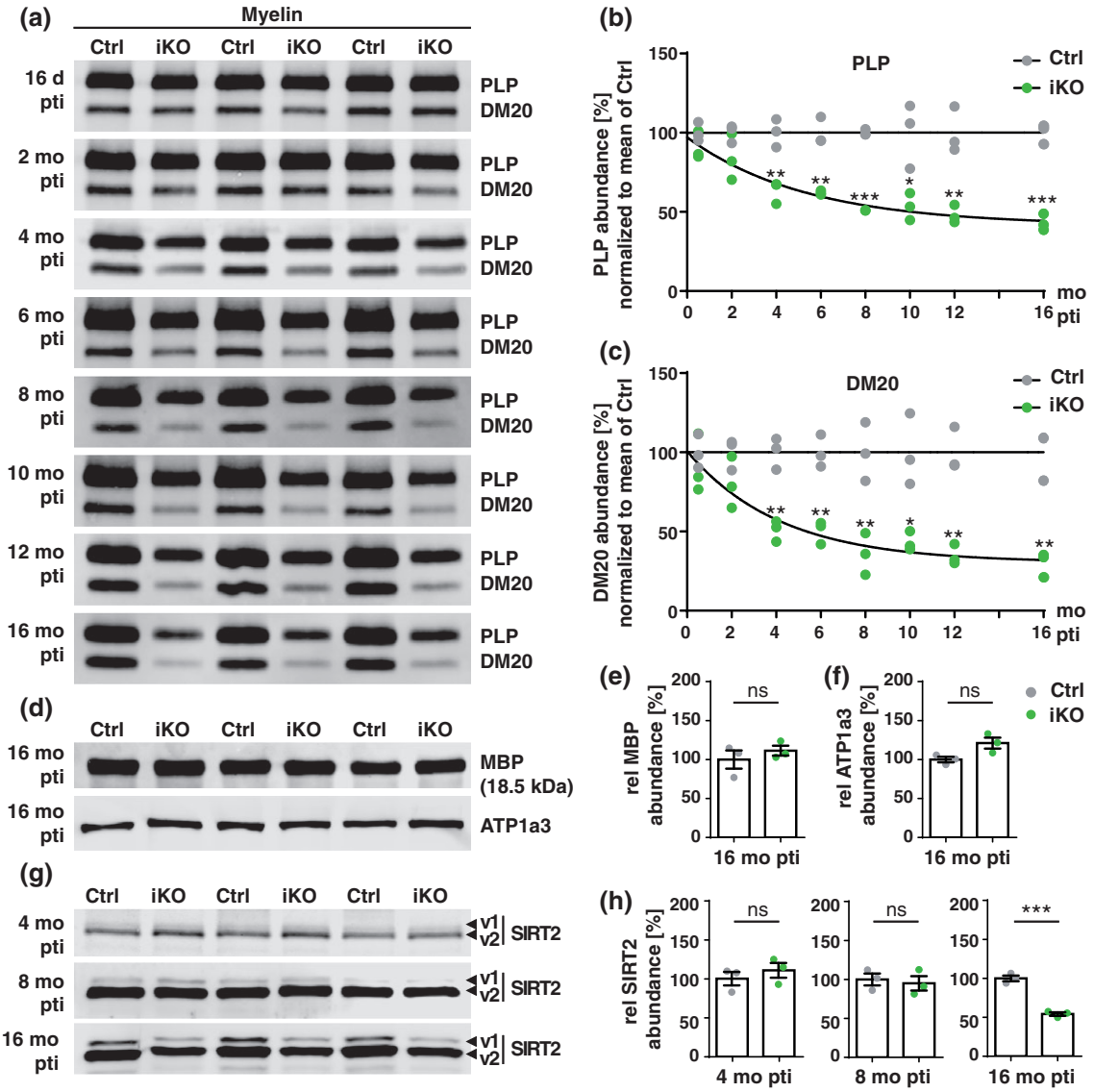

FIGURE 2 Turnover of PLP/DM20 in CNS myelin. (a–c) Immunoblot to detect PLP and its smaller isoform DM20 in myelin biochemically purified from the brains of Ctrl and iKO mice at time points 16 days, 2, 4, 6, 8, 10, 12, and 16 months pti. The abundance of PLP (b) and DM20 (c) in iKO and Ctrl myelin is plotted normalized to the mean of the respective age-matched Ctrl. The decreasing abundance over time of both PLP and DM20 resembles a fitted exponential curve with one-phase decay. *t*-test was performed for each time point individually between iKO and age-matched Ctrl mice. (d–f) Immunoblot to detect MBP and ATP1a3 in myelin purified from the brains of Ctrl and iKO mice at 16 months pti. Quantification of MBP (e) and ATP1a3 (f) abundance detects no significant difference between Ctrl and iKO mice. (g, h) Immunoblot to detect SIRT2 in myelin purified from the brains of Ctrl and iKO mice 4, 8 and 16 months pti. (h) Quantification reveals that the abundance of SIRT2 in myelin is not altered 4 or 8 months pti but significantly reduced in iKO compared with Ctrl mice 16 months pti. Ctrl = control ($Plp^{flox/Y}$); iKO = induced conditional knockout ($Plp^{flox/Y}$*$Plp^{CreERT2}$); mean with *SEM*; $n = 3$; two-tailed unpaired *t*-test; $p < .05$ (*), $p < .01$ (**), and $p < .001$ (***)

$p = .1511$ (2 months pti), $p = .0049$ (4 months pti), $p = .0016$ (6 months pti), $p < .0001$ (8 months pti), $p = .0218$ (10 months pti), $p = .0045$ (12 months pti), and $p = .0003$ (16 months pti). For comparison of the abundance of DM20 in Figure 2c *p*-values are $p = .5022$ (16d pti), $p = .1456$ (2 months pti), $p = .0020$ (4 months pti), $p = .0024$ (6 months pti), $p = .0081$ (8 months pti), $p = .0138$ (10 months pti), $p = .0018$ (12 months pti), and $p = .0022$ (16 months pti). For comparison of the abundance of MBP in Figure 2e, the *p*-value is $p = .4404$. For comparison of the abundance of ATP1a3 in Figure 2f, the *p*-value is $p = .0551$. For comparison of the abundance of SIRT2 in Figure 2h, *p*-values are $p = .4527$ (4 months pti), $p = .6991$ (8 months pti), and $p = .0004$ (16 months pti). For comparison of the abundance of CNP in Supporting Information Figure S1b, the *p*-value is $p = .0412$.

2.4 | Cryo-immuno electron microscopy

Immunogold labeling of cryosections was performed as described in (Patzig, Erwig, et al., 2016). Optic nerves were dissected from three Ctrl and iKO mice each. Primary antibodies were specific for PLP (A431; 1:300; (Jung et al., 1996)). Sections were analyzed with a LEO EM912 Omega (Zeiss, Oberkochen, Germany). Per animal, 41–58

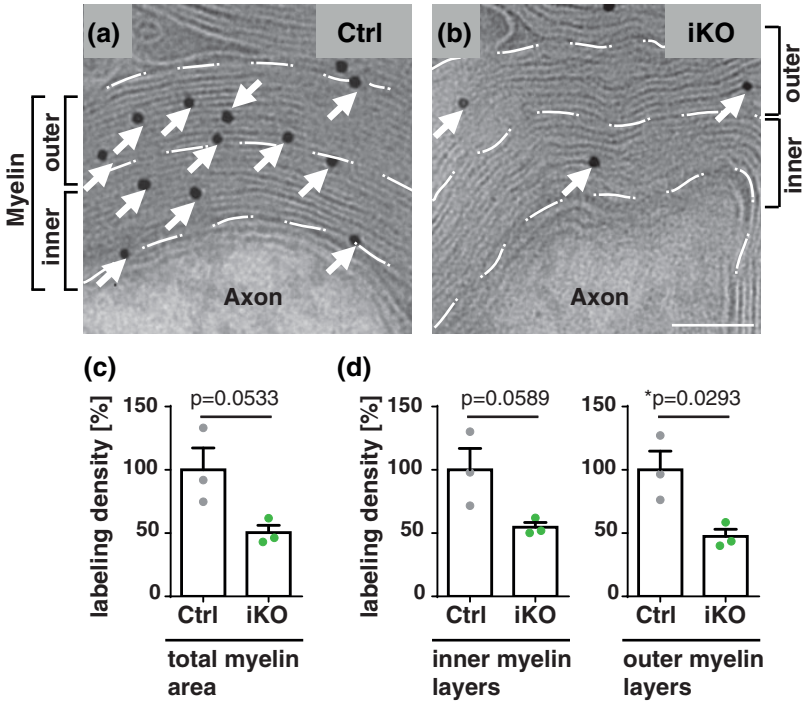

FIGURE 3 Turnover of PLP in optic nerve myelin by cryo-immuno electron microscopy. (a, b) Representative electron micrographs of PLP immunogold labeling on optic nerve cross sections dissected from Ctrl (a) and iKO mice (b) 4 months pti. White arrows point at immunogold particles. Scale bar 75 nm. Inner and outer myelin layers are indicated by stippled lines. (c) Quantification of the density of immunogold particles in compact myelin in Ctrl and iKO optic nerves normalized to the mean of Ctrl mice. (d) Same as in (c) but displayed separately for the inner and outer myelin layers. Note that immunogold labeling in iKO optic nerve myelin is reduced to a similar level in inner and outer myelin layers. Ctrl = control ($Plp^{flox/Y}$); iKO = induced conditional knockout ($Plp^{flox/Y}$*$Plp^{CreERT2}$); mean with *SEM*; $n = 3$; two-tailed unpaired *t*-test; $p < .05$ (*)

myelin profiles were analyzed using Fiji. This corresponds to 3.4–8.4μm^2 myelin area analyzed per animal. The inside and outside half of the compact myelin area were selected and gold-particles on these areas were counted. Graphs display gold particles per μm^2 myelin normalized to mean of Ctrl. All quantifications were performed blinded to the genotype. Statistical analysis was performed using a two-tailed unpaired *t*-test in GraphPad Prism 6.0. Level of significance was set as $p < .05$ (*). Exact *p*-values are given in Figure 3.

2.5 | Immunohistochemistry

Neuropathological analysis by immunohistochemistry was performed as described (de Monasterio-Schrader et al., 2013). In brief, 5–7 male Ctrl and iKO mice per genotype were perfused with 4% PFA at 16 days or 4, 6–8, 10, and 16 months pti. For comparison, 3–10 male wildtype and $Plp^{null/Y}$ mice were perfused at the age of 26 weeks. Brains were dissected, postfixed in 4% PFA for 24 hr and stored in 1% PFA until embedding in paraffin using the Microm HMP110 tissue processor. Brains were sectioned into 5 μm sections using the Microm HM400R Microtome. Immunohistochemical detection of neuropathological markers was performed using the kits $LSAB_2$ (DAKO) and Vector Elite ABC (Vector labs). Antibodies were specific for MAC3 (1:400; Pharmingen 553322; clone M3/84), IBA1 (1:1,000; Wako 019-19741), CD3 (1:150; Serotec MCA1477), APP (1:1,000; Millipore MAB 348), or GFAP (1:200; Novocastra NCL-GFAP-GA5). Images were captured at 10x (CD3), 20x (GFAP, IBA1, MAC3), 40x (APP), or 100x (representative images for display in the figures) magnification using a bright-field light microscope (Zeiss AxioImager Z1) coupled to a Zeiss AxioCam MRc camera controlled by Zeiss ZEN 1.0 software and processed using Fiji.

To quantify axonal spheroids and T-lymphocytes, the hippocampal fimbriae were selected and APP$^+$ axonal spheroids and CD3$^+$ T-lymphocytes were counted, respectively. To quantify white matter area immunopositive for IBA1, MAC3 or GFAP, fimbriae were selected and analyzed using an ImageJ plug-in (de Monasterio-Schrader et al., 2013) for semi-automated analysis. CD3$^+$ cells were counted on five non-adjacent slides per animal at 4 months pti, on seven slides per animal at 6–8 months pti, on four slides per animal at 10 months pti, and on two slides per animal at 16 months pti (Figure 7a). For 6 months old wild type animals, two slides per animal were counted and for $Plp^{null/Y}$ mice, 1–2 slides per animal were counted (Figure 7c). All other markers were analyzed on one slide per animal (Figures 5 and 6). For each animal, the mean of both fimbriae was calculated. All quantifications were performed blinded to the genotype. Statistical analysis was performed using a two-tailed unpaired *t*-test in GraphPad Prism 6.0. Levels of significance were set as $p < .05$ (*), $p < .01$ (**), and $p < .001$ (***).

For statistical assessment of APP$^+$ axonal spheroids quantified in the hippocampal fimbria comparing Ctrl versus iKO mice as displayed in Figure 5a, *p*-values are as follows: $p = .1988$ (4 months pti), $p = .0005$ (6–8 months pti), $p < .0001$ (10 months pti), and $p < .0001$ (16 months pti). For comparison of APP$^+$ axonal spheroids in 6 months old, Wt versus $Plp^{null/Y}$ mice displayed in Figure 5c, the *p*-value is $p < .0001$. For quantification of the relative size of area occupied by IBA1$^+$ microglia in Figure 6a, *p*-values are as follows: Ctrl versus iKO

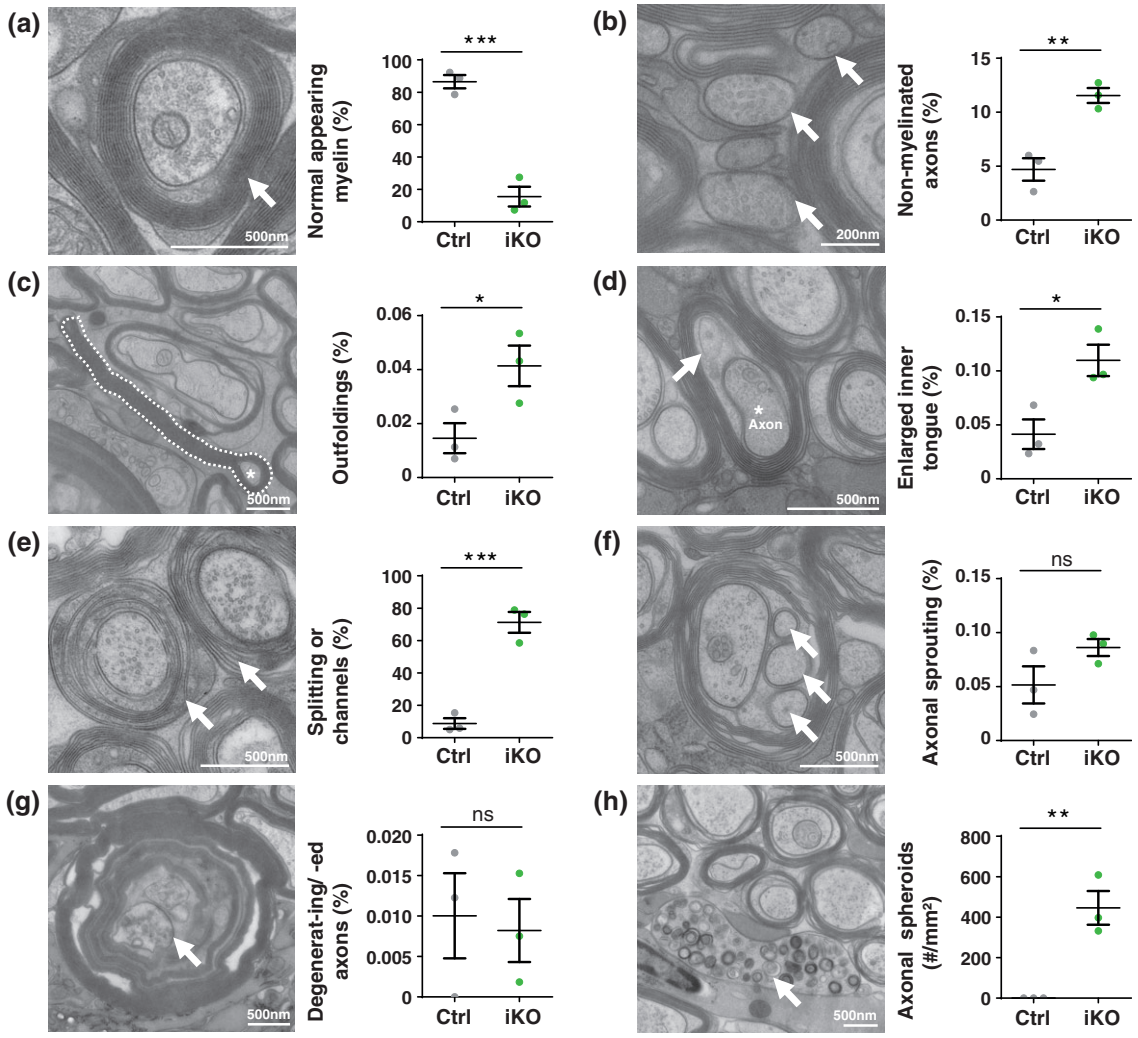

FIGURE 4 Pathology of axon/myelin-units in the optic nerve upon *Plp*-deletion. (a–h) Representative electron micrographs of optic nerve cross sections dissected from Ctrl and iKO mice 10 months pti and genotype-dependent quantification. (a) Normal-appearing axon/myelin-units (arrow). (b) Nonmyelinated axons / internodes (arrows). (c) Myelin outfoldings (white stippled line; asterisk indicates corresponding axon). (d) Enlarged inner tongue (swollen-appearing adaxonal compartment; asterisk indicates axon). (e) Axon/myelin-units with myelin lamellae splittings or myelinic channels. Note that all quantified features of myelin pathology (b–e) are significantly more frequent in iKO compared with Ctrl mice. (f,g) Axon/myelin-units comprising axonal sproutings (f) or degenerating/degenerated axons (g) are present at similar frequencies in Ctrl and iKO mice. In (a–g), numbers of events are expressed as percent of axon/myelin-units assessed on an area of 1,105 μm^2 optic nerve per animal. (h) Axonal spheroids (white arrow) are significantly more frequent in iKO than in Ctrl mice. Axonal spheroids were quantified on at least 18,000 μm^2 per animal and are expressed as number per mm^2. No axonal spheroids were observed in Ctrl mice. Ctrl = control ($Plp^{flox/Y}$); iKO = induced conditional knockout ($Plp^{flox/Y}$*$Plp^{CreERT2}$); mean with *SEM*; $n = 3$; two-tailed unpaired *t*-test; $p < .05$ (*), $p < .01$ (**), and $p < .001$ (***)

4 months pti $p = .1044$, Ctrl versus iKO 6–8 months pti $p = .0058$, Ctrl versus iKO 10 months pti $p = .0621$, Ctrl versus iKO 16 months pti $p = .0003$ and displayed in Figure 5c, the p-value is: Wt versus $Plp^{null/Y}$ 6 months $p < .0001$. For quantification of the relative size of area occupied by $MAC3^+$ microglia in Figure 6d, *p*-values are as follows: Ctrl versus iKO 4 months pti $p = .5551$, Ctrl versus iKO 6–8 months pti $p = .0326$, Ctrl versus iKO 10 months pti $p = .0021$, Ctrl versus iKO 16 months pti $p = .0002$ and displayed in Figure 5f, the p-value is: Wt versus $Plp^{null/Y}$ 6 months $p = .0034$. For quantification of the relative size of area occupied by $GFAP^+$ astrocytes in Figure 6g, *p*-values are as follows: Ctrl versus iKO 4 months pti $p = .0787$, Ctrl versus iKO 6–8 months pti = .0008, Ctrl versus. iKO 10 months pti = .1912, Ctrl versus iKO 16 months pti $p = .0018$ and displayed in Figure 5i, the *p*-value is: Wt versus $Plp^{null/Y}$ 6 months $p = .0066$. For quantification of $CD3^+$ T-cells in Figure 7a, *p*-values are as follows: Ctrl versus iKO 4 months pti $p = .3280$, Ctrl versus iKO 6–8 months pti = .8601, Ctrl versus iKO 10 months pti = .0016, Ctrl versus iKO 16 months pti $p = .0011$ and displayed in Figure 6c, the p-value is: Wt versus $Plp^{null/Y}$ 6 months $p = .0215$.

2.6 | Preparation of CNS mononuclear cells and flow cytometry

FACS analysis was performed as described (Lagumersindez-Denis et al., 2017). In brief, mice were injected i.p. with heparin (5 IU/g body weight); 15 min later, they were perfused transcardially with 20 ml HBSS. Brains were excised and the meninges were removed. The tissue was dissected and digested for 45 min at 37°C with 2.5 mg/ml

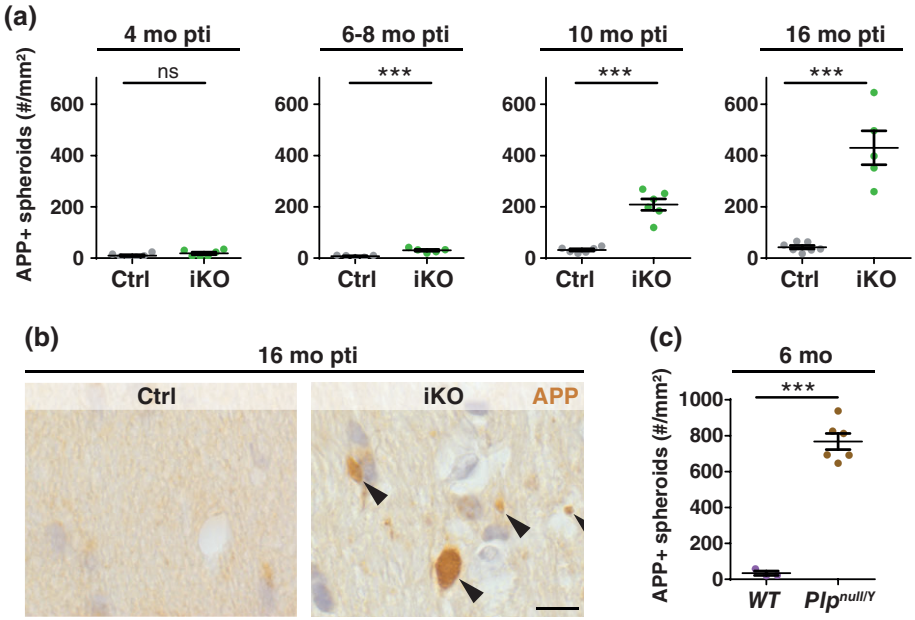

FIGURE 5 Axonal spheroids in the fimbria upon tamoxifen-induced *Plp*-deletion. (a) Genotype-dependent quantification of the frequency of axonal spheroids immunopositive for APP in the hippocampal fimbria at 4, 6–8, 10, and 16 months pti. Note that at the latter time points pti the number of APP-immunopositive (APP^+) axonal spheroids is increased in iKO mice compared with Ctrl mice. (b) Light microscopic images of representative cross-sectioned fimbriae immunolabeled for APP. Scale bar 10 μm. (c) For comparison, in fimbriae of 6-months old $Plp^{null/Y}$ mice the number of APP^+ axonal spheroids is significantly increased compared with age-matched wild type mice. Ctrl = control ($Plp^{flox/Y}$); iKO = induced conditional knockout ($Plp^{flox/Y}$*$Plp^{CreERT2}$); APP = amyloid precursor protein; mean with *SEM*; n = 3–7; two-tailed unpaired t-test; $p < .001$(***)

collagenase D (Roche) and 1 mg/ml DNAse I (Roche) in DMEM. Mononuclear cells were isolated using Percoll gradient centrifugation (37%/70%, GE Healthcare, Chicago, IL), removed from the interphase, washed and blocked with αCD16/32 (BioLegend, Clone 93) for 15 min on ice. The following antibodies were used: αCD3 (145-2C11), αCD4 (RM4-5), αCD8 (53-6.7), αCD11b (M1/70), αCD19 (eBio1D3, eBioscience), αCD25 (PC61.5), αCD45 (30-F11), αFoxP3 (FJK-16S, eBioscience), αLy6C (HK1.4), αLy6G (1A8), αCCR2 (R&D 475301) (BioLegend, if not stated otherwise). For intracellular αFoxP3 labeling, cells were fixed after surface staining for 45 min and permeabilized for 30 min using the eBioscience FoxP3 staining kit. All flow cytometry data were acquired on a FACS Canto™ II (BD Bioscience) and analyzed using FlowJo software (v. 7.6.1, Tree Star Inc., Ashland, OR). Statistical analysis was performed using two-tailed unpaired t-test in GraphPad Prism 6.0. Level of significance was set as $p < .05$ (*).

Immune cells were defined as follows: Microglia: $CD45^{int}$ $CD11b^+$ $Ly6C^-$ $Ly6G^-$; T-cells: $CD45^{high}$ $CD3^+$ $CD19^-$; $CD4^+$ T-cells: $CD45^{high}$ $CD3^+$ $CD4^+$; Regulatory T-cells (T_{reg} cells): $CD45^{high}$ $CD3^+$ $CD4^+$ $CD25^+$ $FoxP3^+$; $CD8^+$ T-cells: $CD45^{high}$ $CD3^+$ $CD8^+$; B-cells: $CD45^{high}$ $CD19^+$ $CD3^-$. For quantification in Figure 7e–l, precise p-values are as follows: $CD3^+$ cells in Figure 7e: $p = .0318$, microglia in Figure 7f: $p = .0171$, $CD8^+$ cells in Figure 7h: $p = .0332$, $CD4^+$ cells in Figure 7i: $p = .1280$, reg T cells in Figure 7k: $p = .2205$, B cells in Figure 7l: $p = .9333$.

2.7 | Electron microscopy

Sample preparation by high pressure-freezing and freeze substitution for transmission electron microscopy was essentially as described (Möbius et al., 2010; Möbius, Nave, & Werner, 2016; Patzig, Kusch, et al., 2016). After sacrificing mice by cervical dislocation, optic nerves were dissected and placed into aluminum specimen carriers with an indentation of 0.2 mm. Remaining space was covered with 20% polyvinylpyrrolidone (Sigma-Aldrich P2307-100G) in PBS. The sample was cryofixed using a HPM100 high-pressure freezer (Leica, Vienna, Austria) and freeze substitution was carried out in a Leica AFS (Leica, Vienna, Austria) according to the following protocol: first, samples were kept in tannic acid (0.1% in acetone) at −90°C for 100 hr, then washed with acetone (4x 30 min, −90°C) and afterward transferred into OsO_4 (EMS; 2%) and uranyl acetate (SPI Chem, 0.1%) in acetone at −90°C. The temperature was raised from −90 to −20°C in increments of 5°C/hr, then kept at −20°C for 16 hr and then raised to +4°C in increments of 10°C/hr. After washing with acetone (3x 30 min at 4°C), samples were allowed to adjust to room temperature for 1 hr. Afterward, optic nerves were transferred into Epon (Serva, Heidelberg, Germany) (25%, 50% and 75% Epon in acetone for 1–2 hr each, 90% Epon in acetone for 18 hr, 100% Epon for 4 hr. Finally, the samples were placed in embedding molds for polymerization (60°C, 24 hr). Ultrathin sections (50 nm) were cut using a Leica Ultracut S ultramicrotome (Leica, Vienna, Austria) and contrasted with an aqueous solution of 4% uranyl acetate (SPI Chem) followed by lead citrate according to (Reynolds, 1963). Samples were examined in a LEO 912AB Omega transmission electron microscope (Zeiss, Oberkochen). Pictures were taken with an on-axis 2048 x 2048-CCD-camera (TRS, Moorenweis, Germany).

For assessment of pathology, three Ctrl and three iKO mice were analyzed 10 months pti. Randomly selected, nonoverlapping images were taken at 7,000x magnification. Per animal, five electron micrographs (1,105μm^2) were analyzed using ImageJ (Fiji). Myelinated and nonmyelinated axons/internodes were categorized into "normal appearing myelin", "myelin with cytoplasmic channels or lamellae

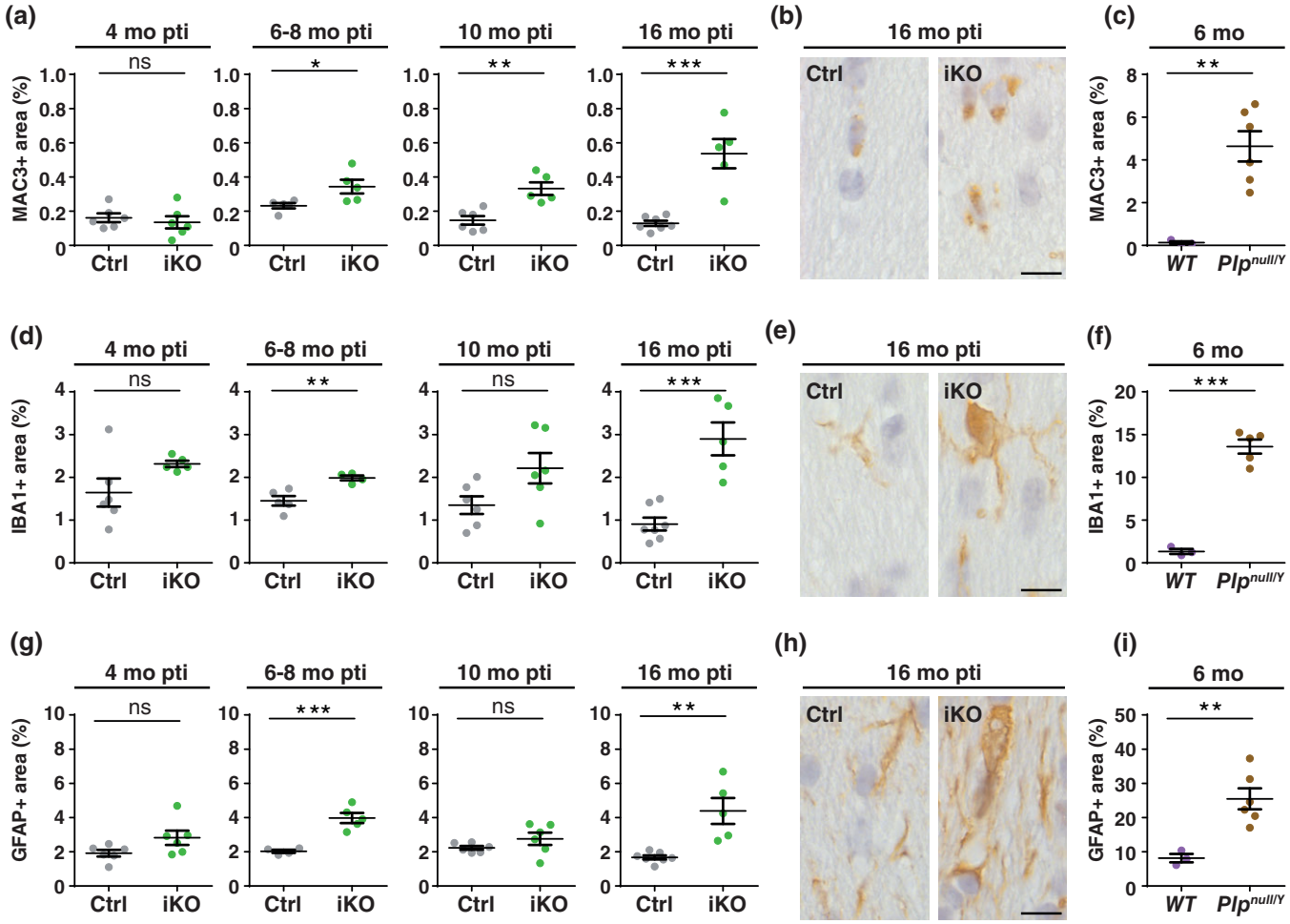

FIGURE 6 Microglial activation and astrogliosis upon tamoxifen-induced *Plp*-deletion. (a, d, g) Genotype-dependent quantification of the relative area of the hippocampal fimbria immunopositive for the microglial markers MAC3 (a) and IBA1 (d) or the astroglial marker GFAP (g) at 4, 6–8, 10, and 16 months pti. (b, e, h) Representative light microscopic images of cross-sectioned fimbriae immunolabeled for IBA1 (b), MAC3 (e) and GFAP (h) in Ctrl and iKO mice at 16 months pti. Scale bar 10 μm. (c, f, i) Quantification of the relative area of the hippocampal fimbria immunopositive for IBA1 (c), MAC3 (f) and GFAP (i) in 6 months old wild type and $Plp^{null/Y}$ mice. Note that the area immunopositive for all three markers is increased in $Plp^{null/Y}$ compared with wild type mice and in iKO compared with Ctrl mice at 6–8 and 16 months pti. Ctrl = control ($Plp^{flox/Y}$); iKO = induced conditional knockout ($Plp^{flox/Y}$*$Plp^{CreERT2}$); IBA1 = allograft-inflammatory factor (AIF1/IBA1); MAC3 = lysosomal-associated membrane protein 2 (LAMP2/MAC3); GFAP = glial fibrillary acidic protein; mean with *SEM*; n = 3–7; two-tailed unpaired t-test; $p < .01$ (**), and $p < .001$(***)

splitting" and "nonmyelinated axons"; these categories were expressed as percent of all assessed axonal profiles. Furthermore, we quantified axon/myelin-profiles in the categories "myelin comprising a swollen adaxonal compartment (inner tongue)", "myelin outfoldings", "profiles with degenerating or degenerated axons" and expressed the number of these events in percent of all profiles counted. The number of axon/myelin-units harboring additional axonal profiles ("axons with sproutings") was expressed as percentage of assessed axons/myelin-units. To quantify axonal spheroids at least 20 images taken at 3,000x magnification (at least 18,000μm^2) per animal were analyzed. The number of axonal spheroids was standardized to the area analyzed for each individual animal and expressed as axonal spheroids/mm^2. All statistical analyses were performed using GraphPad Prism 6.0. Levels of significance were set as $p < .05$ (*), $p < .01$ (**), and $p < .001$ (***). All quantifications were performed blinded to the genotype.

For quantification of myelin and axonal pathology in high pressure frozen optic nerves of Ctrl versus iKO mice in Figure 4, p-values are as follows: normal appearing myelin in Figure 4a: $p = .1404$, nonmyelinated axons in Figure 4b: $p = .0055$, outfoldings in Figure 7c: $p = .0455$, enlarged inner tongue in Figure 7d: $p = .0268$, lamellae splitting or myelin channels in Figure 7e: $p = .0010$, axonal sproutings in Figure 7f: p = .1404, degenerating or degenerated axons in Figure 7g: $p = .7951$, axonal spheroids in Figure 7h: $p = .0059$.

Sample preparation for transmission electron microscopy shown in Supporting Information Figure S2 was performed by conventional aldehyde fixation as described (Werner et al., 2013).

3 | EXPERIMENTAL DESIGN AND STATISTICAL ANALYSIS

Specifications of animals used for the analysis are given in section 2.1. For all quantifications, n numbers represent individual mice and are

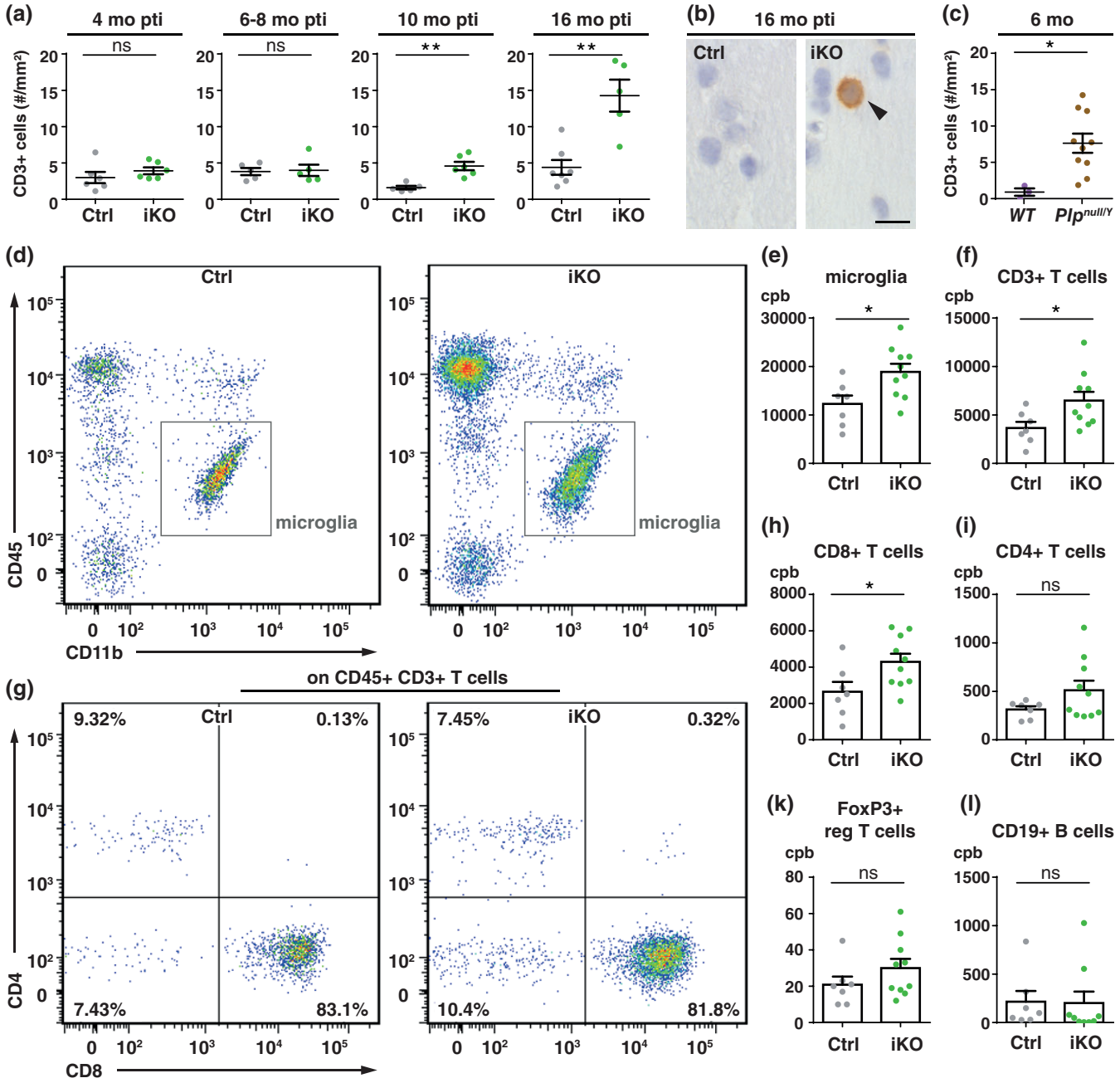

FIGURE 7 Density and markers of T-cells after tamoxifen-induced *Plp*-deletion. (a) Genotype-dependent quantification of the number of CD3-immunopositive ($CD3^+$) T-cells in the fimbria at 4, 6–8, 10, and 16 months pti. Note that the number of $CD3^+$ T-cells is significantly increased in iKO compared with Ctrl mice 10 and 16 months pti. (b) Representative light microscopic images of the hippocampal fimbria immunolabeled for CD3 to detect T-cells 16 months pti. Scale bar 10 μm. (c) For comparison, $CD3^+$ T-cells were quantified in the fimbria of 6 months old $Plp^{null/Y}$ and wild type mice. (a, c) Mean with *SEM*; n = 3–10; two-tailed unpaired t-test; $p < .05$(*), $p < .01$(**). (d) Fluorescence-activated cell sorting (FACS) analysis of cells isolated from the brains of Ctrl and iKO mice 12–17 months pti. The graphs show representative dot plots of CD45 and CD11b flow cytometry; grey boxes highlight microglial cells ($CD45^{int}$ $CD11b^+$). (e, f) Genotype-dependent quantification of $CD45^{int}$ $CD11b^+$ microglia (e) and $CD3^+$ T-cells (f), which are significantly more frequent in iKO compared with Ctrl mice. (g) Quantification of cells isolated by FACS from mouse brains shows that $CD8^+$ T-cells are the dominant T-cell subset and that their numbers are significantly increased in iKO compared with Ctrl mice (h). Numbers of $CD4^+$ T-cells (i), $FoxP3^+$ T_{reg}-cells (k) and B-cells (l) are not altered in iKO compared with Ctrl mice. (e, f, h–l) Mean with *SEM*; n = 7–10; two-tailed unpaired t-test; $p < .01$(**). cpb = cells per brain; Ctrl = control ($Plp^{flox/Y}$); iKO = induced conditional knockout ($Plp^{flox/Y}$*$Plp^{CreERT2}$)

specified in the respective figure legends. In the figures, data points represent individual mice, with the exception of the exemplification of the FACS analysis in Figure 7d,g, in which data points represent sorted cells. All bar graphs display mean with *SEM*. Statistical assessment was performed by two-tailed unpaired t-test using GraphPad Prism 6.0. Levels of significance were set as $p < .05$ (*), $p < .01$ (**), and $p < .001$ (***). Exact p-values are given in section 2.

4 | RESULTS

The abundance of PLP in myelin is exceptionally high in the normal adult CNS; however, the functional relevance of this high steady state level is unknown. Here, we asked if reducing the abundance of PLP in adult mice has functional or neuropathological consequences. To achieve mice in which the *Plp* gene can be inactivated in mature oligodendrocytes in a temporally controlled manner, we crossbred mice harboring a floxed *Plp* allele (Lüders et al., 2017) with transgenic mice expressing tamoxifen-inducible Cre^{ERT2} under control of the *Plp* promoter ($Plp^{CreERT2}$ mice [Leone et al., 2003]), yielding experimental $Plp^{flox/Y}{*}Plp^{CreERT2}$ mice and $Plp^{flox/Y}$ controls. Males of both genotypes were injected i.p. with tamoxifen at 8 weeks of age and sacrificed for analyses 16 days, 2, 4, 6, 8, 10, 12, or 16 months post tamoxifen injection (pti) (Figure 1a). Indeed, PCR genotyping shows that the floxed allele was recombined in $Plp^{flox/Y}{*}Plp^{CreERT2}$ mice after injection of tamoxifen but not without tamoxifen (Figure 1b). For simplicity, we refer to tamoxifen-injected $Plp^{flox/Y}{*}Plp^{CreERT2}$ mice as induced conditional knockout mice (iKO) and to tamoxifen-injected $Plp^{flox/Y}$ mice as controls (Ctrl). To validate that recombination of the *Plp* gene after tamoxifen administration affects its expression, we measured the relative abundance of *Plp* mRNA in the brains of Ctrl and iKO mice. Indeed, by qRT-PCR *Plp* mRNA was strongly reduced in iKO brains at all analyzed time points (Figure 1c). The relative abundance of the mRNA encoding myelin basic protein (MBP) was measured as a control and found unchanged (Figure 1d).

To investigate the dynamics of the change in abundance of PLP and its smaller isoform (Nave, Lai, Bloom, & Milner, 1987) termed DM20 in myelin subsequent to recombining the *Plp*-gene in mature oligodendrocytes, we biochemically purified a myelin-enriched fraction from the brains of iKO and Ctrl mice for assessment by immunoblot (Figure 2a). The abundance of PLP (Figure 2b) and DM20 (Figure 2c) in myelin declined slowly over time, reaching significance by 4 months pti and at all subsequent analysis time points. Four months pti, the abundance of PLP and DM20 was 63 and 51%, respectively, in myelin purified from iKO compared with Ctrl mice. The graphs resembled fitted exponential curves; by 16 months pti, the abundance of PLP and DM20 approached 40 and 30%, respectively, in iKO compared with Ctrl myelin. The marker proteins MBP (Nawaz, Schweitzer, Jahn, & Werner, 2013) and ATP1a3 were detected as controls 16 months pti (Figure 2d); their abundance was unaltered (Figure 2e,f). Considering that the NAD^+-dependent deacetylase sirtuin 2 (SIRT2) is virtually absent from myelin when PLP is lacking constitutively in $Plp^{null/Y}$ mice (Werner et al., 2007), we assessed its abundance in myelin purified from the brains of iKO and Ctrl mice 4, 8, and 16 months pti (Figure 2g). Interestingly, quantification of immunoblots shows that the reduction of the abundance of SIRT2 in iKO myelin reaches significance by 16 months pti (Figure 2h) and thus surprisingly late after that of PLP/DM20. Together, the abundance of PLP and DM20 in myelin declines slowly after recombination of the *Plp* gene in mature oligodendrocytes, reaching significance 4 months pti and reduction by half about 6 months pti.

We then employed cryo-immuno electron microscopy to assess the abundance of PLP at the level of individual myelin sheaths. When applying specific antibodies and protein-A coupled 10 nm gold particles to sectioned optic nerves 4 months pti, PLP was readily detectable in Ctrl myelin (Figure 3a) and, at reduced density, in iKO myelin (Figure 3b). Indeed, quantification of gold particles revealed that the mean abundance of PLP labeling on iKO myelin was about 50% compared with Ctrl myelin, notwithstanding that this trend did not reach the significance threshold of $p < .05$ (Figure 3c). In an attempt to distinguish whether the abundance of PLP declines toward the adaxonal or the abaxonal side of the myelin sheath, we separately quantified PLP-immunogold density on the inner and outer half of the compacted myelin layers (Figure 3d). However, the density of PLP-immunogold particles was approximately similar in the inner (55%) and outer (47%) myelin layers of iKO compared with Ctrl mice. Cryo-immuno electron microscopy thus did not allow distinguishing if the declining PLP abundance occurs toward adaxonal or abaxonal myelin, possibly owing to a high lateral mobility of the protein within the myelin membrane. Together, the abundance of PLP in iKO myelin is about halved by 6 months pti compared with controls according to both immunoblot of total brain myelin and cryo-immuno electron microscopy of individual myelin sheaths. This implies that the half-life of PLP in mature myelin is about 6 months.

To determine if reducing the abundance of PLP in myelin is sufficient to affect the myelin ultrastructure similar to complete PLP-deficiency in $Plp^{null/Y}$ mice, we assessed the optic nerves of iKO and Ctrl mice 10 months pti by electron microscopy after high pressure freezing and freeze substitution. Indeed, the frequency of normal-appearing axon/myelin-units was strongly reduced in iKO mice (Figure 4a). Considering the increased frequency of non-myelinated axons/internodes in $Plp^{null/Y}$ mice (de Monasterio-Schrader et al., 2013; Yool et al., 2001), we quantified this feature in iKO mice. Indeed, the frequency of nonmyelinated axons/internodes is increased in iKO compared with Ctrl mice 10 months pti (Figure 4b). Myelin outfoldings were recently reported as a neuropathological feature in $Plp^{null/Y}$ mice (Patzig, Erwig, et al., 2016), and our quantification reveals that their frequency is also increased in iKO compared with Ctrl mice (Figure 4c). Enlarged adaxonal myelin layers (Figure 4d) and the presence of split myelin lamellae or non-compacted cytoplasmic channels through compacted myelin sheaths (Figure 4e) were also more frequent in iKO compared with Ctrl mice. According to quantitative immunoblotting of myelin purified from the brains of iKO and Ctrl mice 4 months pti, the enlargement of these non-compacted myelin subcompartments in iKO mice correlated with an increased abundance of CNP (Supporting Information Figure S1), a marker protein for non-compacted myelin (Edgar et al., 2009; Snaidero et al., 2017). Together, all previously identified pathological ultrastructural features of $Plp^{null/Y}$ myelin do also emerge secondarily (see also Supporting Information Figure S2) when the abundance of PLP in myelin is reduced upon recombining the *Plp* gene in the adult CNS.

Considering that $Plp^{null/Y}$ mice display axonal degeneration (de Monasterio-Schrader et al., 2013; Edgar et al., 2004; Griffiths et al., 1998; Lüders et al., 2017; Patzig, Erwig, et al., 2016) qualifying them as a model of SPG2 caused by *PLP1* gene mutations in humans, we asked if reducing the abundance of PLP in myelin is sufficient to cause a similar axonopathy. Although the frequency of axon/myelin-units comprising axonal sproutings (Figure 4f) or advanced or

complete axonal degeneration was not elevated in iKO compared with Ctrl mice (Figure 4g), axonal spheroids emerged as frequent in iKO mice by 10 months pti (Figure 4h). It is noteworthy that axonal spheroids are the most prominent feature of axonal pathology in iKO mice (Figure 4h), *Plp*$^{null/Y}$ mice and SPG2 patients (de Monasterio-Schrader et al., 2013; Garbern et al., 2002; Griffiths et al., 1998; Werner et al., 2013), whereas they are virtually absent in Ctrl mice (Figure 4h).

To assess the temporal dynamics of the emerging axonopathy, iKO and Ctrl mice were sacrificed at various ages and their brains were subjected to neuropathological analysis by immunohistochemistry using amyloid precursor protein (APP) as a marker. The hippocampal fimbria was selected for quantitative assessment because it is a comparatively uniform white matter tract through which the long axons of excitatory neurons project (Li, Fang, Fernandez, & Pleasure, 2013; Lüders et al., 2017). A small number of APP^{+} axonal spheroids was detected in the brains of iKO mice already 4 months pti, reaching significance 6–8 months pti and further increasing at later time points (Figure 5a,b). For comparison, the number of APP^{+} axonal spheroids in 6 months old *Plp*$^{null/Y}$ mice (Figure 5c) was higher compared with iKO mice (Figure 5a), which is expected when considering that the former are lacking PLP throughout life. We note that the emergence of axonal spheroids in the brains of iKO mice precedes the reduction of the abundance of SIRT2 in myelin (Figure 2g,h), which may argue against a major role for oligodendroglial expression of SIRT2 in preventing axonal pathology.

Considering that the axonopathy in *Plp*$^{null/Y}$ mice is accompanied by astrogliosis and microglial activation (de Monasterio-Schrader et al., 2013), the brains of iKO and Ctrl mice were subjected to immunohistochemistry using the microglial markers MAC3 and IBA1 (ionized calcium-binding adaptor molecule 1) and the astrocytic marker GFAP (glial fibrillary acidic protein). When assessing the hippocampal fimbria we observed an increased area of immunopositivity in iKO mice, which reached significance 6–8 months pti and further increased at later time points (Figure 6, Supporting Information Figure S3). Together, temporal dynamics of the emerging axonopathy was similar to that of the reactive astrogliosis and microgliosis. A clearly pro-inflammatory or pro-regenerative microglia marker gene expression profile was not evident according to qRT-PCR (Supporting Information Figure S4).

Axonal pathology and gliosis may be accompanied by the infiltration of T-lymphocytes (de Monasterio-Schrader et al., 2013; Lüders et al., 2017). To quantitatively assess T-lymphocytes in the present model, the brains of iKO and Ctrl mice were subjected to immunohistochemistry using CD3 as a marker. Indeed, quantitative assessment of the hippocampal fimbria revealed that the number of T-lymphocytes was increased in iKO compared with Ctrl mice. Interestingly, this first reached significance 10 months pti (Figure 7a,b) and thus later than the increased number of axonal spheroids, astrogliosis and microgliosis. Together, iKO mice display the entire spectrum of neuropathology also observed in *Plp*$^{null/Y}$ mice. However, different from mice constitutively lacking PLP, iKO mice allow the temporal dissection of the emerging neuropathology. These findings imply that T-lymphocytes infiltrate the brains of iKO mice subsequent to axonopathy, microgliosis, and astrogliosis.

Finally, we used multicolor flow cytometry to characterize immune cells in more detail. Cells were isolated from whole brains of iKO and Ctrl mice 12–17 months pti, immunolabeled and separated by fluorescence-activated cell sorting (FACS). Density plots of cells immunopositive for the markers CD45 or CD11b indicate that microglia/macrophages are more numerous in iKO compared with Ctrl mice (Figure 7d). Indeed, quantification confirms an increased number of microglia (CD45^{int} CD11b^{+}) in the brains of iKO mice (Figure 7e), in agreement with the neuropathological assessment of the fimbria using the markers MAC3 and IBA1 (Figure 6). FACS also confirmed that CD3^{+} T-lymphocytes are more frequent in the brains of iKO compared with Ctrl mice (Figure 7f), in agreement with the quantitative immunohistochemistry (Figure 7a,b). To characterize the subtypes of T-lymphocytes present in our model, we quantified CD4^{+} and CD8^{+} T-cells. CD8^{+} cells, which are frequently described as cytotoxic T-cells, are the dominant lymphocyte population in the analyzed brains (Figure 7g). Moreover, their number is significantly increased in the brains of iKO compared with Ctrl mice (Figure 7h). Trends toward increased numbers of CD4^{+} cells (Figure 7i), which are frequently viewed as T-helper cells, as well as of FoxP3^{+} regulatory T-lymphocytes (T_{regs}) (Figure 7k) did not reach significance. The number of CD19^{+} B-cells was low in both iKO and Ctrl mice; genotype-dependent differences were not evident (Figure 7l).

5 | DISCUSSION

We report the first mouse model in which the *Plp*-gene is recombined in mature oligodendrocytes by temporally controlled injection of tamoxifen in adult mice, thereby terminating the replenishment of PLP in mature myelin sheaths. In effect, the abundance of PLP in CNS myelin declines by half within 6 months probably reflecting its slow turnover. Notably, the reduced PLP-abundance was sufficient to cause the entire spectrum of pathological changes that affect the CNS when PLP is lacking completely in PLP-related disorders. It was striking that axonopathy and gliosis preceded the infiltration of CD8^{+} T-cells.

5.1 | Turnover and persistence of PLP in adult CNS myelin

A previous metabolic pulse-chase labeling approach has found PLP, MBP, CNP, SIRT2, and other myelin proteins among the most long-lived proteins in entire rat brains, together with nucleoporins and histones (Toyama et al., 2013). It is commonly believed that these proteins are replaced only slowly despite their robust expression owing to their localization in structures that are turned over slowly, such as nuclear pore complexes or myelin sheaths. Six months after the end of the dietary ^{15}N isotope labeling pulse, the fractional abundance of PLP peptides comprising the ^{15}N label was 18.5%, suggesting that about one out of five PLP molecules persisted for this period. However, the experiment may not serve well as an approximation for the turnover rate of PLP and myelin in the adult CNS because (a) the dietary pulse was applied in the first 6 weeks after birth, the most active phase of myelin biogenesis that also involves considerable

developmental shortening and retraction of myelin sheaths (Baraban, Koudelka, & Lyons, 2018; Krasnow, Ford, Valdivia, Wilson, & Attwell, 2018), and (b) the experiment was not designed to discriminate PLP molecules in myelin sheaths from those in oligodendroglial cell bodies, which most probably have rather different turnover rates. Thus, we believe that the measured value of 18.5% ^{15}N-containing PLP-related peptides after 6 months (Toyama et al., 2013) represents an underestimation when assumed to reflect the persistence of PLP in adult myelin.

The turnover of myelin and oligodendrocytes has also been measured in human brains using the levels of the carbon isotope ^{14}C from the fallout of nuclear bomb tests in the 1950s and 1960s as a worldwide labeling pulse (Yeung et al., 2014). Analyzing ^{14}C incorporation in the nuclear DNA of oligodendrocytes sorted from the corpus callosum derived from autopsy material revealed that almost all oligodendrocytes emerged in the first 5 years of life and later displayed a very slow but continuous replacement rate. Conversely, the ^{14}C concentration in myelin biochemically purified from the brains of the subjects was largely similar to the atmospheric ^{14}C concentration at the time of death. Although the experiment did not allow calculating a particular rate for the exchange of PLP or myelin it has established that, different from oligodendroglial nuclei, myelin is indeed turned over in the human white matter in the time-course of a few years or less. Together, these pulse-chase experiments have indicated that oligodendrocytes remodel their myelin over time.

A complex molecular program is required for the maintenance of myelin, including the continued expression of signal-transducing proteins and transcription factors essential for the expression of numerous myelin-related genes (Nave & Werner, 2014). This was recently confirmed upon tamoxifen-induced deletion of the transcription factor myelin regulatory factor (MRF) and of the extracellular signal-regulated kinases-1 and -2 (ERK1/2) in adult mice (Ishii, Furusho, Dupree, & Bansal, 2014; Koenning et al., 2012). In the brains of $Mrf^{flox/flox}{*}Plp^{CreERT2}$ mice (Koenning et al., 2012), severe demyelination was evident by 8 weeks pti, probably a consequence of both oligodendroglial apoptosis and of surviving oligodendrocytes losing their ability to maintain their myelin sheaths. Notably, the abundance of *Plp*-mRNA declined considerably within 1 week pti in the brains of these mice, thereby displaying one of the strongest reactions among the tested myelin-related genes. However, the severe demyelination in $Mrf^{flox/flox}{*}Plp^{CreERT2}$ mice prevents conclusions about the normal turnover of PLP or myelin. $Erk1^{null/null}{*}Erk2^{flox/flox}{*}Plp^{CreERT2}$ mice (Ishii et al., 2014) displayed severe demyelination 6 months pti, probably owing to reduced expression of *Mrf*, *Mbp* and other transcripts essential for normal myelin biogenesis. Importantly, axonal degeneration was also observed in these mice, a possible consequence of the reduced expression of *Plp*, *Cnp* and other myelin genes involved in oligodendrocyte-to-axon support.

The present model provides a system with no or only minimal demyelination in which the abundance of PLP in CNS myelin was measured after terminating its replenishment by temporally controlled induced recombination of the *Plp*-gene. Reduction by half was achieved about six months pti, both in myelin biochemically purified from total brains (Figure 2a–c) and individual myelin sheaths in the optic nerve (Figure 3). We note that this apparent half-life represents an approximation to the turnover of PLP in healthy mature myelin considering that various factors affect the measured values in either direction. For example, splitting of myelin lamellae, itself a consequence of the reduced PLP-abundance, may in turn increase the lateral mobility of PLP, thereby enhancing its degradation and further accelerating the declining PLP-abundance. In contrast, the continued differentiation of oligodendrocyte progenitor cells in adult mice leads to the emergence of a number of adult-born mature oligodendrocytes (Auer, Vagionitis, & Czopka, 2018; Hill, Li, & Grutzendler, 2018; Hughes, Kang, Fukaya, & Bergles, 2013; McKenzie et al., 2014; Tripathi et al., 2017; Yeung et al., 2014; Young et al., 2013); according to our experimental design using the $Plp^{CreERT2}$ driver line (Leone et al., 2003) it is expected that their newly formed myelin sheaths contain PLP. Over time, the PLP present in the newly formed myelin sheaths of these adult-born oligodendrocytes will sum up to represent a portion of the biochemically purified myelin fraction visible by immunoblotting. Together, in the present experimental approach the turnover of PLP in CNS myelin may be moderately over- or underestimated. It may also vary in dependence of species, brain region and age. Yet, the observed pathology of myelin and axons emerges as a direct consequence of the reduced PLP-abundance in CNS myelin.

5.2 | Continuous high level of PLP is necessary to maintain the ultrastructure of CNS myelin

The spatio-temporal expression of the *Plp*-gene and the very high abundance of its gene product in CNS myelin imply that PLP has a critical function for myelination. Yet, PLP is not essential for the biogenesis of myelin per se when considering that substantial amounts of myelin develop when PLP is lacking in humans or mice (Garbern et al., 1997; Klugmann et al., 1997). Yet, the developmental rate of myelination is moderately reduced in $Plp^{null/Y}$ mice (de Monasterio-Schrader et al., 2013; Yool et al., 2001). Considering that myelination continues in adult mice we interpret the moderately increased frequency of non-myelinated axons/internodes in the present model 10 months pti (Figure 4b) as impaired myelin biogenesis rather than demyelination of previously myelinated axons.

Various defects affect the ultrastructure and stability of myelin when PLP is lacking constitutively, including pathological outfoldings of entire myelin sheaths (Patzig, Erwig, et al., 2016), fused-appearing intraperiod lines and lamellae splittings (Boison, Bussow, D'Urso, Muller, & Stoffel, 1995; Klugmann et al., 1997; Möbius et al., 2008; Möbius et al., 2016). We have noted that similar defects also emerge when the *Plp*-gene is recombined in mature oligodendrocytes. In particular, the strikingly high frequency of axon/myelin profiles with lamellae splittings (Figure 4e) implies that PLP, beyond its involvement in myelin biogenesis per se, is also required to maintain myelin ultrastructure and stability. Lamellae splittings and cytosolic channels through otherwise compact myelin could not always be distinguished morphologically and may even represent two manifestations of the same phenomenon. Indeed, PLP appears to function as an adhesive molecular strut in myelin (Duncan, Hammang, & Trapp, 1987; Kitagawa, Sinoway, Yang, Gould, & Colman, 1993) notwithstanding that it lacks any features of classical adhesion proteins. Considering the comparatively subtle adhesive properties that PLP exerts, at least in vitro

(Bakhti et al., 2013; Bizzozero, Bixler, Davis, Espinosa, & Messier, 2001), a sufficiently large number of PLP molecules in myelin is required to stabilize compact myelin in vivo. The present study provides evidence that a mere reduction of the abundance of PLP in myelin is sufficient to cause the emergence of cytosolic channels through CNS myelin as well as susceptibility to widespread lamellae splitting. This implies that the high content of PLP in CNS myelin of tetrapods is subject to selective pressure, which maintains myelin stability.

5.3 | Continuous high level of PLP in myelin is required to prevent axonopathy and secondary neuropathology

Generalized, loss-of-function mutations of the *PLP1/Plp*-gene impair the biogenesis and stability of myelin and axonal integrity as observed in SPG2 and $Plp^{null/Y}$ mice; gain-of-function mutations additionally cause demyelination and oligodendrocyte death (Duncan, Kondo, & Zhang, 2011; Garbern, 2007; Gruenenfelder, Thomson, Penderis, & Edgar, 2011; Werner et al., 1998; Woodward, 2008), as seen in the leukodystrophy Pelizaeus-Merzbacher disease (PMD) (Saugier-Veber et al., 1994) and its models including $Plp^{transgenic\text{-}overexpressor}$ mice (Edgar et al., 2010; Kagawa et al., 1994; Readhead, Schneider, Griffiths, & Nave, 1994; Tanaka et al., 2009) and rats (Mayer, Larsen, Kondo, & Duncan, 2011), Plp^{Jimpy} (Cerghet, Bessert, Nave, & Skoff, 2001; Gotow et al., 1999; Rosenfeld & Freidrich Jr., 1983; Schneider et al., 1992) and transgenic PLP^{L30R} and PLP^{R137W} mice (Groh et al., 2016), the $Plp^{shaking\text{-}pup/Y}$ spaniel dog (Mayer et al., 2015) and the myelin-deficient (Plp^{md}) rat (Duncan et al., 1987; Miller et al., 2003). The severe and rapidly progressive demyelination in the latter models has made it difficult to dissect the chronological order and thus neuropathological hierarchy of the emerging neuropathology.

While gliosis and infiltrating T-cells were previously observed in the brains of $Plp^{null/Y}$ mice (de Monasterio-Schrader et al., 2013; Lüders et al., 2017) and other PLP-related disorders (Marteyn & Baron-Van Evercooren, 2016), in the present model axonal spheroids and secondary neuropathology emerge within months when the *Plp*-gene is recombined in mature oligodendrocytes. Although it was impossible to temporally uncouple axonal spheroids from gliosis, our results indicate that axonal pathology precedes the infiltration of T-cells. Importantly, genetic and pharmacological intervention has shown that infiltrating T-cells accelerate axonal degeneration in the $Plp^{transgenic\text{-}overexpressor}$ (Ip et al., 2006; Ip et al., 2012), PLP^{L30R} and PLP^{R137W} (Groh et al., 2016) transgenic mouse models of PMD caused by overexpression or missense mutations of the *Plp*-gene, respectively. Interestingly, experimental ablation of T-cells was effective in reducing but did not completely prevent axonal pathology. Generalized, in a spectrum of PLP-related disorders axonal pathology precedes infiltrating T-cells which in turn enhance axonal degeneration, suggesting that T-cells are not the primary cause of but rather accelerate the axonopathy. Considering that myelin and axon pathology are not simply a developmental defect in our model, we speculate that it might in principle be possible to reverse at least some of the pathology in individuals harboring *PLP1* null mutations by restoring gene expression after disease onset.

In conclusion, reducing the abundance of PLP in adult CNS myelin causes widespread neuropathology, suggesting that the high-level content of PLP is subject to selective pressure. Considering the low abundance of PLP in peripheral myelin and in the CNS of fish (Patzig et al., 2011; Yoshida & Colman, 1996), the requirement of PLP for the functions of myelinating oligodendrocytes in preventing the degeneration of myelinated axons is specific to the CNS of tetrapods.

ACKNOWLEDGMENTS

We thank A. Fahrenholz and U. Kutzke for technical support, M. Eichel for discussions, and U. Suter for mice. $Plp^{Cre\text{-}ERT2}$ mice were used in collaboration with U. Suter. Our work is supported by the Cluster of Excellence and Deutsche Forschungsgemeinschaft (DFG) Research Center Nanoscale Microscopy and Molecular Physiology of the Brain (W.M. and K.-A.N), the DFG (grants WE 2720/2-2 and WE 2720/4-1 to H.B.W.) and the ERC (advanced grant to K.-A.N.).

ORCID

Wiebke Möbius https://orcid.org/0000-0002-2902-7165
Klaus-Armin Nave https://orcid.org/0000-0001-8724-9666
Hauke B. Werner https://orcid.org/0000-0002-7710-5738

REFERENCES

Auer, F., Vagionitis, S., & Czopka, T. (2018). Evidence for myelin sheath remodeling in the CNS revealed by in vivo imaging. *Current Biology*, *28*(4), 549–559.e543. https://doi.org/10.1016/j.cub.2018.01.017

Bakhti, M., Snaidero, N., Schneider, D., Aggarwal, S., Möbius, W., Janshoff, A., … Simons, M. (2013). Loss of electrostatic cell-surface repulsion mediates myelin membrane adhesion and compaction in the central nervous system. *Proceedings of the National Academy of Sciences of the United States of America*, *110*(8), 3143–3148. https://doi.org/10.1073/pnas.1220104110

Baraban, M., Koudelka, S., & Lyons, D. A. (2018). Ca (2+) activity signatures of myelin sheath formation and growth in vivo. *Nature Neuroscience*, *21*(1), 19–23. https://doi.org/10.1038/s41593-017-0040-x

Bizzozero, O. A., Bixler, H. A., Davis, J. D., Espinosa, A., & Messier, A. M. (2001). Chemical deacylation reduces the adhesive properties of proteolipid protein and leads to decompaction of the myelin sheath. *Journal of Neurochemistry*, *76*(4), 1129–1141. https://doi.org/10.1046/j.1471-4159.2001.00116.x

Boison, D., Bussow, H., D'Urso, D., Müller, H. W., & Stoffel, W. (1995). Adhesive properties of proteolipid protein are responsible for the compaction of CNS myelin sheaths. *The Journal of Neuroscience*, *15*(8), 5502–5513. https://doi.org/10.1523/JNEUROSCI.15-08-05502.1995

Cerghet, M., Bessert, D. A., Nave, K. A., & Skoff, R. P. (2001). Differential expression of apoptotic markers in jimpy and in plp overexpressors: Evidence for different apoptotic pathways. *Journal of Neurocytology*, *30*(9–10), 841–855.

de Monasterio-Schrader, P., Jahn, O., Tenzer, S., Wichert, S. P., Patzig, J., & Werner, H. B. (2012). Systematic approaches to central nervous system myelin. *Cellular and Molecular Life Sciences*, *69*(17), 2879–2894. https://doi.org/10.1007/s00018-012-0958-9

de Monasterio-Schrader, P., Patzig, J., Möbius, W., Barrette, B., Wagner, T. L., Kusch, K., … Werner, H. B. (2013). Uncoupling of neuroinflammation from axonal degeneration in mice lacking the myelin protein tetraspanin-2. *Glia*, *61*(11), 1832–1847. https://doi.org/10.1002/glia.22561

Duncan, I. D., Hammang, J. P., & Trapp, B. D. (1987). Abnormal compact myelin in the myelin-deficient rat: Absence of proteolipid protein correlates with a defect in the intraperiod line. *Proceedings of the National*

Academy of Sciences of the United States of America, *84*(17), 6287–6291. https://doi.org/10.1073/pnas.84.17.6287

Duncan, I. D., Kondo, Y., & Zhang, S. C. (2011). The myelin mutants as models to study myelin repair in the leukodystrophies. *Neurotherapeutics*, *8*(4), 607–624. https://doi.org/10.1007/s13311-011-0080-y

Edgar, J. M., McCulloch, M. C., Montague, P., Brown, A. M., Thilemann, S., Pratola, L., … Nave, K. A. (2010). Demyelination and axonal preservation in a transgenic mouse model of Pelizaeus-Merzbacher disease. *EMBO Molecular Medicine*, *2*(2), 42–50. https://doi.org/10.1002/emmm.200900057

Edgar, J. M., McLaughlin, M., Werner, H. B., McCulloch, M. C., Barrie, J. A., Brown, A., … Griffiths, I. R. (2009). Early ultrastructural defects of axons and axon-glia junctions in mice lacking expression of cnp1. *Glia*, *57*(16), 1815–1824. https://doi.org/10.1002/glia.20893

Edgar, J. M., McLaughlin, M., Yool, D., Zhang, S. C., Fowler, J. H., Montague, P., … Griffiths, I. R. (2004). Oligodendroglial modulation of fast axonal transport in a mouse model of hereditary spastic paraplegia. *The Journal of Cell Biology*, *166*(1), 121–131. https://doi.org/10.1083/jcb.200312012

Folch, J., & Lees, M. (1951). Proteolipides, a new type of tissue lipoproteins; their isolation from brain. *The Journal of Biological Chemistry*, *191*(2), 807–817.

Franz, T., Waehneldt, T. V., Neuhoff, V., & Wachtler, K. (1981). Central nervous system myelin proteins and glycoproteins in vertebrates: A phylogenetic study. *Brain Research*, *226*(1–2), 245–258. https://doi.org/10.1016/0006-8993(81)91097-0

Garbern, J. Y. (2007). Pelizaeus-Merzbacher disease: Genetic and cellular pathogenesis. *Cellular and Molecular Life Sciences*, *64*(1), 50–65. https://doi.org/10.1007/s00018-006-6182-8

Garbern, J. Y., Cambi, F., Tang, X. M., Sima, A. A., Vallat, J. M., Bosch, E. P., … Kamholz, J. (1997). Proteolipid protein is necessary in peripheral as well as central myelin. *Neuron*, *19*(1), 205–218. https://doi.org/10.1016/S0896-6273(00)80360-8

Garbern, J. Y., Yool, D. A., Moore, G. J., Wilds, I. B., Faulk, M. W., Klugmann, M., … Griffiths, I. R. (2002). Patients lacking the major CNS myelin protein, proteolipid protein 1, develop length-dependent axonal degeneration in the absence of demyelination and inflammation. *Brain*, *125*(Pt 3), 551–561.

Gotow, T., Leterrier, J. F., Ohsawa, Y., Watanabe, T., Isahara, K., Shibata, R., … Uchiyama, Y. (1999). Abnormal expression of neurofilament proteins in dysmyelinating axons located in the central nervous system of jimpy mutant mice. *The European Journal of Neuroscience*, *11*(11), 3893–3903. https://doi.org/10.1046/j.1460-9568.1999.00820.x

Gould, E. A., Busquet, N., Shepherd, D., Dietz, R. M., Herson, P. S., Simoes de Souza, F. M., … Macklin, W. B. (2018). Mild myelin disruption elicits early alteration in behavior and proliferation in the subventricular zone. *eLife*, *7*, pii: e34783. https://doi.org/10.7554/eLife.34783

Griffiths, I., Klugmann, M., Anderson, T., Yool, D., Thomson, C., Schwab, M. H., … Nave, K. A. (1998). Axonal swellings and degeneration in mice lacking the major proteolipid of myelin. *Science*, *280*(5369), 1610–1613. https://doi.org/10.1126/science.280.5369.1610

Groh, J., Friedman, H. C., Orel, N., Ip, C. W., Fischer, S., Spahn, I., … Martini, R. (2016). Pathogenic inflammation in the CNS of mice carrying human plp1 mutations. *Human Molecular Genetics*, *25*(21), 4686–4702. https://doi.org/10.1093/hmg/ddw296

Gruenenfelder, F. I., Thomson, G., Penderis, J., & Edgar, J. M. (2011). Axon-glial interaction in the CNS: What we have learned from mouse models of Pelizaeus-Merzbacher disease. *Journal of Anatomy*, *219*(1), 33–43. https://doi.org/10.1111/j.1469-7580.2011.01363.x

Hill, R. A., Li, A. M., & Grutzendler, J. (2018). Lifelong cortical myelin plasticity and age-related degeneration in the live mammalian brain. *Nature Neuroscience*, *21*(5), 683–695. https://doi.org/10.1038/s41593-018-0120-6

Hughes, E. G., Kang, S. H., Fukaya, M., & Bergles, D. E. (2013). Oligodendrocyte progenitors balance growth with self-repulsion to achieve homeostasis in the adult brain. *Nature Neuroscience*, *16*(6), 668–676. https://doi.org/10.1038/nn.3390

Ip, C. W., Kroner, A., Bendszus, M., Leder, C., Kobsar, I., Fischer, S., … Martini, R. (2006). Immune cells contribute to myelin degeneration and axonopathic changes in mice overexpressing proteolipid protein in oligodendrocytes. *The Journal of Neuroscience*, *26*(31), 8206–8216. https://doi.org/10.1523/JNEUROSCI.1921-06.2006

Ip, C. W., Kroner, A., Groh, J., Huber, M., Klein, D., Spahn, I., … Martini, R. (2012). Neuroinflammation by cytotoxic T-lymphocytes impairs retrograde axonal transport in an oligodendrocyte mutant mouse. *PLoS One*, *7*(8), e42554. https://doi.org/10.1371/journal.pone.0042554

Ishii, A., Furusho, M., Dupree, J. L., & Bansal, R. (2014). Role of erk1/2 mapk signaling in the maintenance of myelin and axonal integrity in the adult CNS. *The Journal of Neuroscience*, *34*(48), 16031–16045. https://doi.org/10.1523/JNEUROSCI.3360-14.2014

Jahn, O., Tenzer, S., Bartsch, N., Patzig, J., & Werner, H. B. (2013). Myelin proteome analysis: Methods and implications for the myelin cytoskeleton. *Neuromethods*, *79*, 335–353. https://doi.org/10.1007/978-1-62703-266-7_15

Jahn, O., Tenzer, S., & Werner, H. B. (2009). Myelin proteomics: Molecular anatomy of an insulating sheath. *Molecular Neurobiology*, *40*(1), 55–72. https://doi.org/10.1007/s12035-009-8071-2

Janova, H., Arinrad, S., Balmuth, E., Mitjans, M., Hertel, J., Habes, M., … Nave, K. A. (2018). Microglia ablation alleviates myelin-associated catatonic signs in mice. *The Journal of Clinical Investigation*, *128*(2), 734–745. https://doi.org/10.1172/JCI97032

Jung, M., Sommer, I., Schachner, M., & Nave, K. A. (1996). Monoclonal antibody O10 defines a conformationally sensitive cell-surface epitope of proteolipid protein (PLP): Evidence that PLP misfolding underlies dysmyelination in mutant mice. *The Journal of Neuroscience*, *16*(24), 7920–7929. https://doi.org/10.1523/JNEUROSCI.16-24-07920.1996

Kagawa, T., Ikenaka, K., Inoue, Y., Kuriyama, S., Tsujii, T., Nakao, J., … Mikoshiba, K. (1994). Glial cell degeneration and hypomyelination caused by overexpression of myelin proteolipid protein gene. *Neuron*, *13*(2), 427–442. https://doi.org/10.1016/0896-6273(94)90358-1

Kirschner, D. A., Inouye, H., Ganser, A. L., & Mann, V. (1989). Myelin membrane structure and composition correlated: A phylogenetic study. *Journal of Neurochemistry*, *53*(5), 1599–1609. https://doi.org/10.1111/j.1471-4159.1989.tb08558.x

Kitagawa, K., Sinoway, M. P., Yang, C., Gould, R. M., & Colman, D. R. (1993). A proteolipid protein gene family: Expression in sharks and rays and possible evolution from an ancestral gene encoding a pore-forming polypeptide. *Neuron*, *11*(3), 433–448. https://doi.org/10.1016/0896-6273(93)90148-K

Klugmann, M., Schwab, M. H., Puhlhofer, A., Schneider, A., Zimmermann, F., Griffiths, I. R., & Nave, K. A. (1997). Assembly of CNS myelin in the absence of proteolipid protein. *Neuron*, *18*(1), 59–70. https://doi.org/10.1016/S0896-6273(01)80046-5

Koenning, M., Jackson, S., Hay, C. M., Faux, C., Kilpatrick, T. J., Willingham, M., & Emery, B. (2012). Myelin gene regulatory factor is required for maintenance of myelin and mature oligodendrocyte identity in the adult CNS. *The Journal of Neuroscience*, *32*(36), 12528–12542. https://doi.org/10.1523/JNEUROSCI.1069-12.2012

Krämer-Albers, E. M., Gehrig-Burger, K., Thiele, C., Trotter, J., & Nave, K. A. (2006). Perturbed interactions of mutant proteolipid protein/DM20 with cholesterol and lipid rafts in oligodendroglia: Implications for dysmyelination in spastic paraplegia. *The Journal of Neuroscience*, *26*(45), 11743–11752. https://doi.org/10.1523/JNEUROSCI.3581-06.2006

Krasnow, A. M., Ford, M. C., Valdivia, L. E., Wilson, S. W., & Attwell, D. (2018). Regulation of developing myelin sheath elongation by oligodendrocyte calcium transients in vivo. *Nature Neuroscience*, *21*(1), 24–28. https://doi.org/10.1038/s41593-017-0031-y

Kruger, L., & Maxwell, D. S. (1966). Electron microscopy of oligodendrocytes in normal rat cerebrum. *The American Journal of Anatomy*, *118*(2), 411–435. https://doi.org/10.1002/aja.1001180207

Kusch, K., Uecker, M., Liepold, T., Möbius, W., Hoffmann, C., Neumann, H., … Jahn, O. (2017). Partial immunoblotting of 2D-gels: A novel method to identify post-translationally modified proteins exemplified for the myelin acetylome. *Proteomes*, *5*(1), pii: E3. https://doi.org/10.3390/proteomes5010003

Lagumersindez-Denis, N., Wrzos, C., Mack, M., Winkler, A., van der Meer, F., Reinert, M. C., … Nessler, S. (2017). Differential contribution of immune effector mechanisms to cortical demyelination in multiple sclerosis. *Acta Neuropathologica*, *134*(1), 15–34. https://doi.org/10.1007/s00401-017-1706-x

Leone, D. P., Genoud, S., Atanasoski, S., Grausenburger, R., Berger, P., Metzger, D., … Suter, U. (2003). Tamoxifen-inducible glia-specific CRE mice for somatic mutagenesis in oligodendrocytes and Schwann cells. *Molecular and Cellular Neurosciences*, *22*(4), 430–440. https://doi.org/10.1016/S1044-7431(03)00029-0

Li, G., Fang, L., Fernandez, G., & Pleasure, S. J. (2013). The ventral hippocampus is the embryonic origin for adult neural stem cells in the dentate gyrus. *Neuron*, *78*(4), 658–672. https://doi.org/10.1016/j.neuron.2013.03.019

Lüders, K. A., Patzig, J., Simons, M., Nave, K. A., & Werner, H. B. (2017). Genetic dissection of oligodendroglial and neuronal Plp1 function in a novel mouse model of spastic paraplegia type 2. *Glia*, *65*(11), 1762–1776. https://doi.org/10.1002/glia.23193

Marteyn, A., & Baron-Van Evercooren, A. (2016). Is involvement of inflammation underestimated in Pelizaeus-Merzbacher disease? *Journal of Neuroscience Research*, *94*(12), 1572–1578. https://doi.org/10.1002/jnr.23931

Mayer, J. A., Griffiths, I. R., Goldman, J. E., Smith, C. M., Cooksey, E., Radcliff, A. B., & Duncan, I. D. (2015). Modeling the natural history of Pelizaeus-Merzbacher disease. *Neurobiology of Disease*, *75*, 115–130. https://doi.org/10.1016/j.nbd.2014.12.023

Mayer, J. A., Larsen, E. C., Kondo, Y., & Duncan, I. D. (2011). Characterization of a Plp-overexpressing transgenic rat, a model for the connatal form of Pelizaeus-Merzbacher disease. *Neurobiology of Disease*, *44*(2), 231–238. https://doi.org/10.1016/j.nbd.2011.07.007

McKenzie, I. A., Ohayon, D., Li, H., de Faria, J. P., Emery, B., Tohyama, K., & Richardson, W. D. (2014). Motor skill learning requires active central myelination. *Science*, *346*(6207), 318–322. https://doi.org/10.1126/science.1254960

Miller, M. J., Haxhiu, M. A., Georgiadis, P., Gudz, T. I., Kangas, C. D., & Macklin, W. B. (2003). Proteolipid protein gene mutation induces altered ventilatory response to hypoxia in the myelin-deficient rat. *The Journal of Neuroscience*, *23*(6), 2265–2273. https://doi.org/10.1523/JNEUROSCI.23-06-02265.2003

Milner, R. J., Lai, C., Nave, K. A., Lenoir, D., Ogata, J., & Sutcliffe, J. G. (1985). Nucleotide sequences of two mRNAs for rat brain myelin proteolipid protein. *Cell*, *42*(3), 931–939. https://doi.org/10.1016/0092-8674(85)90289-2

Möbius, W., Cooper, B., Kaufmann, W. A., Imig, C., Ruhwedel, T., Snaidero, N., … Varoqueaux, F. (2010). Electron microscopy of the mouse central nervous system. *Methods in Cell Biology*, *96*, 475–512. https://doi.org/10.1016/S0091-679X(10)96020-2

Möbius, W., Nave, K. A., & Werner, H. B. (2016). Electron microscopy of myelin: Structure preservation by high-pressure freezing. *Brain Research*, *1641*(Pt A), 92–100. https://doi.org/10.1016/j.brainres.2016.02.027

Möbius, W., Patzig, J., Nave, K. A., & Werner, H. B. (2008). Phylogeny of proteolipid proteins: Divergence, constraints, and the evolution of novel functions in myelination and neuroprotection. *Neuron Glia Biology*, *4*(2), 111–127. https://doi.org/10.1017/S1740925X0900009X

Nave, K. A., Lai, C., Bloom, F. E., & Milner, R. J. (1987). Splice site selection in the proteolipid protein (Plp) gene transcript and primary structure of the DM-20 protein of central nervous system myelin. *Proceedings of the National Academy of Sciences of the United States of America*, *84*(16), 5665–5669. https://doi.org/10.1073/pnas.84.16.5665

Nave, K. A., & Werner, H. B. (2014). Myelination of the nervous system: Mechanisms and functions. *Annual Review of Cell and Developmental Biology*, *30*, 503–533. https://doi.org/10.1146/annurev-cellbio-100913-013101

Nawaz, S., Schweitzer, J., Jahn, O., & Werner, H. B. (2013). Molecular evolution of myelin basic protein, an abundant structural myelin component. *Glia*, *61*(8), 1364–1377. https://doi.org/10.1002/glia.22520

Patzig, J., Erwig, M. S., Tenzer, S., Kusch, K., Dibaj, P., Möbius, W., … Werner, H. B. (2016). Septin/anillin filaments scaffold central nervous system myelin to accelerate nerve conduction. *eLife*, *5*, pii: e17119. https://doi.org/10.7554/eLife.17119

Patzig, J., Jahn, O., Tenzer, S., Wichert, S. P., de Monasterio-Schrader, P., Rosfa, S., … Werner, H. B. (2011). Quantitative and integrative proteome analysis of peripheral nerve myelin identifies novel myelin proteins and candidate neuropathy loci. *The Journal of Neuroscience*, *31*(45), 16369–16386. https://doi.org/10.1523/JNEUROSCI.4016-11.2011

Patzig, J., Kusch, K., Fledrich, R., Eichel, M. A., Lüders, K. A., Möbius, W., … Werner, H. B. (2016). Proteolipid protein modulates preservation of peripheral axons and premature death when myelin protein zero is lacking. *Glia*, *64*(1), 155–174. https://doi.org/10.1002/glia.22922

Petit, B., Giraudet, F., Bechon, C., Bardin, L., Avan, P., Boespflug-Tanguy, O., & Begou, M. (2014). Mice with a deletion of the major central myelin protein exhibit hypersensitivity to noxious thermal stimuli: Involvement of central sensitization. *Neurobiology of Disease*, *65*, 55–68. https://doi.org/10.1016/j.nbd.2014.01.005

Philips, T., & Rothstein, J. D. (2017). Oligodendroglia: Metabolic supporters of neurons. *The Journal of Clinical Investigation*, *127*(9), 3271–3280. https://doi.org/10.1172/JCI90610

Readhead, C., Schneider, A., Griffiths, I., & Nave, K. A. (1994). Premature arrest of myelin formation in transgenic mice with increased proteolipid protein gene dosage. *Neuron*, *12*(3), 583–595. https://doi.org/10.1016/0896-6273(94)90214-3

Reynolds, E. S. (1963). The use of lead citrate at high ph as an electron-opaque stain in electron microscopy. *The Journal of Cell Biology*, *17*, 208–212. https://doi.org/10.1083/jcb.17.1.208

Rosenfeld, J., & Freidrich, V. L., Jr. (1983). Axonal swellings in jimpy mice: Does lack of myelin cause neuronal abnormalities? *Neuroscience*, *10*(3), 959–966. https://doi.org/10.1016/0306-4522(83)90233-6

Saab, A. S., Tzvetanova, I. D., & Nave, K. A. (2013). The role of myelin and oligodendrocytes in axonal energy metabolism. *Current Opinion in Neurobiology*, *23*(6), 1065–1072. https://doi.org/10.1016/j.conb.2013.09.008

Saugier-Veber, P., Munnich, A., Bonneau, D., Rozet, J. M., Le Merrer, M., Gil, R., & Boespflug-Tanguy, O. (1994). X-linked spastic paraplegia and Pelizaeus-Merzbacher disease are allelic disorders at the proteolipid protein locus. *Nature Genetics*, *6*(3), 257–262. https://doi.org/10.1038/ng0394-257

Schardt, A., Brinkmann, B. G., Mitkovski, M., Sereda, M. W., Werner, H. B., & Nave, K.-A. (2009). The SNARE protein SNAP-29 interacts with the GTPase rab3a: Implications for membrane trafficking in myelinating glia. *Journal of Neuroscience Research*, *87*, 3465–3479. https://doi.org/10.1002/jnr.22005

Schneider, A., Montague, P., Griffiths, I., Fanarraga, M., Kennedy, P., Brophy, P., & Nave, K. A. (1992). Uncoupling of hypomyelination and glial cell death by a mutation in the proteolipid protein gene. *Nature*, *358*(6389), 758–761. https://doi.org/10.1038/358758a0

Sharma, K., Schmitt, S., Bergner, C. G., Tyanova, S., Kannaiyan, N., Manrique-Hoyos, N., … Simons, M. (2015). Cell type- and brain region-resolved mouse brain proteome. *Nature Neuroscience*, *18*(12), 1819–1831. https://doi.org/10.1038/nn.4160

Simons, M., Kramer, E. M., Thiele, C., Stoffel, W., & Trotter, J. (2000). Assembly of myelin by association of proteolipid protein with cholesterol- and galactosylceramide-rich membrane domains. *The Journal of Cell Biology*, *151*(1), 143–154. https://doi.org/10.1083/jcb.151.1.143

Snaidero, N., Velte, C., Myllykoski, M., Raasakka, A., Ignatev, A., Werner, H. B., … Simons, M. (2017). Antagonistic functions of MBP and CNP establish cytosolic channels in CNS myelin. *Cell Reports*, *18*(2), 314–323. https://doi.org/10.1016/j.celrep.2016.12.053

Tanaka, H., Ma, J., Tanaka, K. F., Takao, K., Komada, M., Tanda, K., … Ikenaka, K. (2009). Mice with altered myelin proteolipid protein gene expression display cognitive deficits accompanied by abnormal neuron-glia interactions and decreased conduction velocities. *The Journal of Neuroscience*, *29*(26), 8363–8371. https://doi.org/10.1523/JNEUROSCI.3216-08.2009

Tasaki, I. (1939). The electro-saltatory transmission of the nerve impulse and the effect of narcosis upon the nerve fiber. *The American Journal of Physiology*, *127*(2), 211–227.

Toyama, B. H., Savas, J. N., Park, S. K., Harris, M. S., Ingolia, N. T., Yates, J. R., 3rd, & Hetzer, M. W. (2013). Identification of long-lived proteins reveals exceptional stability of essential cellular structures. *Cell*, *154*(5), 971–982. https://doi.org/10.1016/j.cell.2013.07.037

Trapp, B. D., Moench, T., Pulley, M., Barbosa, E., Tennekoon, G., & Griffin, J. (1987). Spatial segregation of mRNA encoding myelin-specific proteins. *Proceedings of the National Academy of*

Sciences of the United States of America, *84*(21), 7773–7777. https://doi.org/10.1073/pnas.84.21.7773

Tripathi, R. B., Jackiewicz, M., McKenzie, I. A., Kougioumtzidou, E., Grist, M., & Richardson, W. D. (2017). Remarkable stability of myelinating oligodendrocytes in mice. *Cell Reports*, *21*(2), 316–323. https://doi.org/10.1016/j.celrep.2017.09.050

Waehneldt, T. V. (1990). Phylogeny of myelin proteins. *Annals of the New York Academy of Sciences*, *605*, 15–28. https://doi.org/10.1111/j.1749-6632.1990.tb42377.x

Wang, L., Winnewisser, J., Federle, C., Jessberger, G., Nave, K. A., Werner, H. B., … Hinterberger, M. (2017). Epitope-specific tolerance modes differentially specify susceptibility to proteolipid protein-induced experimental autoimmune encephalomyelitis. *Frontiers in Immunology*, *8*, 1511. https://doi.org/10.3389/fimmu.2017.01511

Werner, H., Jung, M., Klugmann, M., Sereda, M., Griffiths, I. R., & Nave, K. A. (1998). Mouse models of myelin diseases. *Brain Pathology*, *8*(4), 771–793. https://doi.org/10.1111/j.1750-3639.1998.tb00200.x

Werner, H. B., Krämer-Albers, E. M., Strenzke, N., Saher, G., Tenzer, S., Ohno-Iwashita, Y., … Nave, K. A. (2013). A critical role for the cholesterol-associated proteolipids PLP and M6B in myelination of the central nervous system. *Glia*, *61*(4), 567–586. https://doi.org/10.1002/glia.22456

Werner, H. B., Kuhlmann, K., Shen, S., Uecker, M., Schardt, A., Dimova, K., … Nave, K. A. (2007). Proteolipid protein is required for transport of sirtuin 2 into CNS myelin. *The Journal of Neuroscience*, *27*(29), 7717–7730. https://doi.org/10.1523/JNEUROSCI.1254-07.2007

Woodward, K. J. (2008). The molecular and cellular defects underlying Pelizaeus-Merzbacher disease. *Expert Reviews in Molecular Medicine*, *10*, e14. https://doi.org/10.1017/S1462399408000677

Yeung, M. S., Zdunek, S., Bergmann, O., Bernard, S., Salehpour, M., Alkass, K., … Frisen, J. (2014). Dynamics of oligodendrocyte generation and myelination in the human brain. *Cell*, *159*(4), 766–774. https://doi.org/10.1016/j.cell.2014.10.011

Yin, X., Baek, R. C., Kirschner, D. A., Peterson, A., Fujii, Y., Nave, K. A., … Trapp, B. D. (2006). Evolution of a neuroprotective function of central nervous system myelin. *The Journal of Cell Biology*, *172*(3), 469–478. https://doi.org/10.1083/jcb.200509174

Yool, D. A., Klugmann, M., McLaughlin, M., Vouyiouklis, D. A., Dimou, L., Barrie, J. A., … Griffiths, I. R. (2001). Myelin proteolipid proteins promote the interaction of oligodendrocytes and axons. *Journal of Neuroscience Research*, *63*(2), 151–164. https://doi.org/10.1002/1097-4547(20010115)63:2<151::AID-JNR1007>3.0.CO;2-Y

Yoshida, M., & Colman, D. R. (1996). Parallel evolution and coexpression of the proteolipid proteins and protein zero in vertebrate myelin. *Neuron*, *16*(6), 1115–1126. https://doi.org/10.1016/S0896-6273(00)80138-5

Young, K. M., Psachoulia, K., Tripathi, R. B., Dunn, S. J., Cossell, L., Attwell, D., … Richardson, W. D. (2013). Oligodendrocyte dynamics in the healthy adult CNS: Evidence for myelin remodeling. *Neuron*, *77*(5), 873–885. https://doi.org/10.1016/j.neuron.2013.01.006

SUPPORTING INFORMATION

Additional supporting information may be found online in the Supporting Information section at the end of the article.

How to cite this article: Lüders KA, Nessler S, Kusch K, et al. Maintenance of high proteolipid protein level in adult central nervous system myelin is required to preserve the integrity of myelin and axons. *Glia*. 2019;1–16. https://doi.org/10.1002/glia.23549